# Thermal-elastic stresses and the criticality of the continental crust

Geochemistry Geophysics Geosystems G3

Published by AGU and the Geochemical Society

*Article*
Volume 13, Number 9
13 September 2012
Q09005, doi:10.1029/2012GC004085
ISSN: 1525-2027

# Thermal-elastic stresses and the criticality of the continental crust

**C. E. Schrank**
*School of Earth, Environmental and Biological Sciences, Queensland University of Technology, 2 George Street, GPO Box 2434, Brisbane, Queensland 4001, Australia (christoph.schrank@qut.edu.au)*

*Western Australian Geothermal Centre of Excellence, Perth, Western Australia 6009, Australia*

*School of Earth and Environment, University of Western Australia, Perth, Western Australia 6009, Australia*

**F. Fusseis**
*Institut für Geologie, Mineralogie und Geophysik, Ruhr-Universität Bochum, DE-44801 Bochum, Germany*

*Western Australian Geothermal Centre of Excellence, Perth, Western Australia 6009, Australia*

*School of Earth and Environment, University of Western Australia, Perth, Western Australia 6009, Australia*

**A. Karrech**
*School of Civil Engineering, University of Western Australia, Perth, Western Australia 6009, Australia*

*CSIRO Earth Science and Resource Engineering, Perth, Western Australia 6151, Australia*

**K. Regenauer-Lieb**
*Western Australian Geothermal Centre of Excellence, Perth, Western Australia 6009, Australia*

*School of Earth and Environment, University of Western Australia, Perth, Western Australia 6009, Australia*

*CSIRO Earth Science and Resource Engineering, Perth, Western Australia 6151, Australia*

[1] Heating or cooling can lead to high stresses in rocks due to the different thermal-elastic properties of minerals. In the upper 4 km of the crust, such internal stresses might cause fracturing. Yet it is unclear if thermal elasticity contributes significantly to critical stresses and failure deeper in Earth's continental crust, where ductile creep causes stress relaxation. We combined a heating experiment conducted in a Synchrotron microtomograph (Advanced Photon Source, USA) with numerical simulations to calculate the grain-scale stress field in granite generated by slow burial. We find that deviatoric stresses >100 MPa can be stored during burial, with relaxation times from 100's to 1000's ka, even in the ductile crust. Hence, grain-scale thermal-elastic stresses may serve as nuclei for instabilities, thus rendering the continental crust close to criticality.

**Components:** 10,500 words, 13 figures, 5 tables.

**Keywords:** burial; continental crust; criticality; heating; internal stresses; thermal elasticity.

**Index Terms:** 5104 Physical Properties of Rocks: Fracture and flow; 8020 Structural Geology: Mechanics, theory, and modeling; 8164 Tectonophysics: Stresses: crust and lithosphere.

**Received** 2 February 2012; **Revised** 31 July 2012; **Accepted** 10 August 2012; **Published** 13 September 2012.

Schrank, C. E., F. Fusseis, A. Karrech, and K. Regenauer-Lieb (2012), Thermal-elastic stresses and the criticality of the continental crust, *Geochem. Geophys. Geosyst.*, *13*, Q09005, doi:10.1029/2012GC004085.

## 1. Introduction

[2] The seismogenic crust forms the uppermost brittle part of continents where stresses from plate motions are released by earthquakes. The KTB borehole project revealed that the stress state in this part of the western European brittle continental crust is close to critical so that small changes in stress can cause failure [*Zoback et al.*, 1993]. This puzzling observation was attributed to the ridge-push force exerted by the cooling and thickening oceanic lithosphere associated with the Mid-Atlantic Ridge. *Zoback et al.* [1993] predicted that similar stress states can be expected in stable shield areas and relatively old oceanic basins. Here, we explore the idea that an alternative mechanism may contribute significantly to stresses close to failure within continental crust: thermal elasticity. Rocks generally contain minerals with different and/or anisotropic thermal-expansion and elastic properties. Therefore, upon changes in temperature and pressure, contact interactions arise at the grain scale due to geometric mismatch between minerals with different and/or anisotropic thermal-elastic properties [*Fredrich and Wong*, 1986]. These interpenetrative contacts generate deviatoric thermal-elastic, so-called *internal*, stresses. Hitherto, thermal-elastic internal stresses were mainly investigated in the context of cooling brittle rocks, for three reasons. First, they can generate micro-cracks (Figure 1) in the upper ~4 km of the continental crust [e.g., *Heard and Page*, 1982], which affect rock properties such as elasticity, strength, fracture toughness, thermal conductivity, and permeability [*Cooper and Simmons*, 1977; *Meredith and Atkinson*, 1985; *Nasseri et al.*, 2009]. This is relevant for resource extraction (e.g., mining, quarrying, and drilling), nuclear waste disposal, and reservoir stimulation [*Heard and Page*, 1982; *Nasseri et al.*, 2007]. Second, large thermal stresses are expected in cooling oceanic lithosphere [*Parmentier and Haxby*, 1986]. They have been suggested to cause transform faults and earthquakes in the oceanic crust [*Bratt et al.*, 1985; *Turcotte*, 1974] and may even be instrumental to the formation of tectonic plates [*Korenaga*, 2007a]. Finally, thermal-elastic stresses generated by rock exhumation have been invoked for explaining horizontal compressive stresses near Earth's surface [*Bruner*, 1979, 1984; *Nadan and Engelder*, 2009]. Yet it is unclear if thermal elasticity affects the long-term behavior of the thick ductile continental crust, which can deform by temperature-activated creep. It is mostly assumed that, above a critical temperature, thermal-elastic stresses are relaxed quickly by crystal-plastic flow [*Blendell and Coble*, 1982; *Bratt et al.*, 1985; *Bruner*, 1984; *Turcotte and Oxburgh*, 1976]. However, stress relaxation by ductile flow is a time-dependent, slow process while thermal-elastic stresses build up quasi-instantaneously upon temperature and pressure variation. Thus, it is conceivable that, even in the hotter brittle-ductile continental crust, thermal-elastic stresses might reach magnitudes and lifetimes that are sufficient to affect long-term geological processes [*Denlinger and Savage*, 1989; *Korenaga*, 2007a]. This is the hypothesis examined in this paper, using a new hybrid workflow (Figure 1c). The workflow employs a physical heating experiment on Westerly granite conducted in a Synchrotron X-Ray microtomograph to calibrate a mixed finite element/contact-element simulation of grain-scale stresses in the laboratory sample. Subsequently, the calibrated model is applied to simulating thermal-elastic stresses in granitic rock induced by slow burial incorporating published creep laws.

## 2. Experimental Program

[3] Granite is the main constituent of the continental crust, containing its most characteristic minerals: quartz and feldspar. The strength of the continental crust can be characterized by granitic rheology [*Carter and Tsenn*, 1987]. Relatively permeable sedimentary rocks often cover granitic basement.

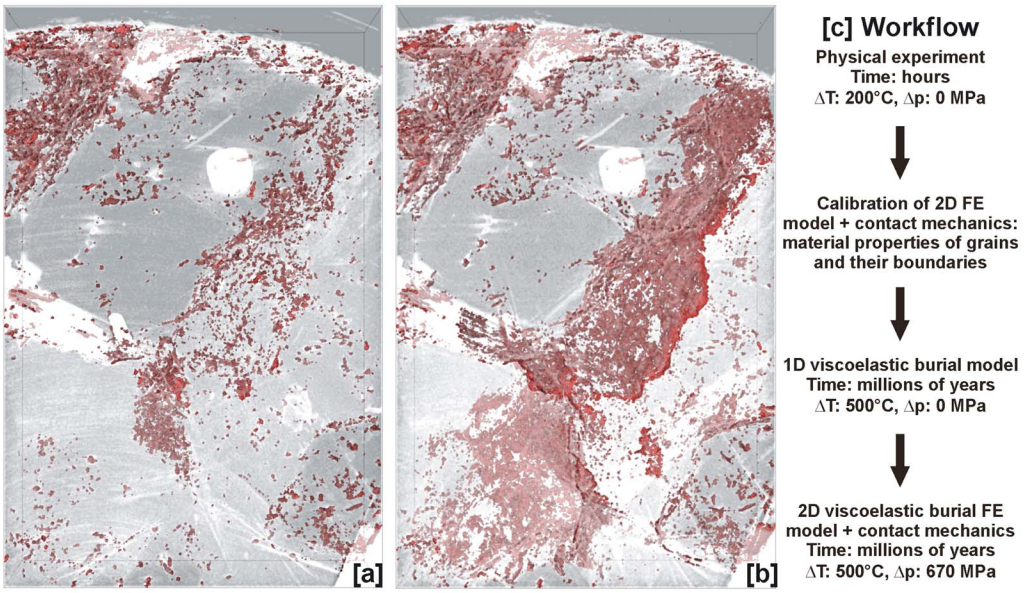


**Figure 1.** (a) 3D rendering of a thick-slice tomogram of the Westerly granite sample prior to heating (at 25°C). Horizontal image width is 650 $\mu$m. Image depth is 130 $\mu$m. The thick slice is cut perpendicular to the long axis of the cylindrical sample. Pre-existing pores and micro-cracks are colored red. (b) Thick slice depicted in Figure 1a after heating to 220°C. Note two large connected grain-boundary cracks extending from the lower left to the upper right of the tomogram. Most of the thermally induced damage clearly concentrates along grain boundaries. (c) Workflow employed here.

Due to their proximity to the surface, thermal expansion in porous media is generally controlled by deformation on shorter time scales [*Ben-Zion and Leary*, 1986] which are beyond the scope of this study. The common geological scenario that inspired our heating experiments is burial: the vertical movement of a rock volume from Earth's cool surface into its hot interior. Rocks experience burial due to isostatic adjustment and/or tectonic transport, for example in filling sedimentary basins, under ice loads during ice ages, in subduction zones, and in active mountain belts.

[4] The low thermal-elastic loading rates associated with rock burial – burial velocities in nature are on the order of millimeters per year [e.g., *Escher and Beaumont*, 1997; *Lapen et al.*, 2003] – cannot be realized in a laboratory experiment. In addition, it is difficult to measure internal stresses directly. Therefore, we employed 1D and 2D numerical models to examine the grain-scale stress field induced by burial. A physical heating experiment of an unconfined granite sample observed with time-lapse 4D Synchrotron X-ray microtomography was used to calibrate the numerical simulations under laboratory conditions. It permitted to monitor the slow expansion of the sample, the internal deformation of its minerals and pore space, and the formation of micro-cracks in 3D in situ, providing direct evidence that heating induces large thermal-elastic stresses (Figures 1a and 1b). The results of the physical heating experiment served to constrain material properties of grain boundaries and minerals of the granite sample in 2D numerical simulations of the laboratory heating experiment. The material properties were then employed in simple 1D numerical viscoelastic models of burial-induced thermal-elastic stresses to illustrate the first-order physics of the problem. Finally, we applied 2D grain-scale finite element models with contact mechanics to account for the effects of microstructure, grain-boundary cracking, simultaneous mechanical and thermal loading, and temperature-dependent viscoelasticity. The remainder of the paper is organized according to this workflow, as summarized in Figure 1c.

## 3. Calibration

[5] A reasonable numerical quantification of the grain-scale stress field induced by burial requires knowledge of the material properties of the constituent minerals and their grain boundaries. It is well known [*Hadley*, 1976], and confirmed by our observations (Figures 1a and 2a), that virgin Westerly granite contains abundant intracrystalline micro-damage, especially in plagioclase. Such voids

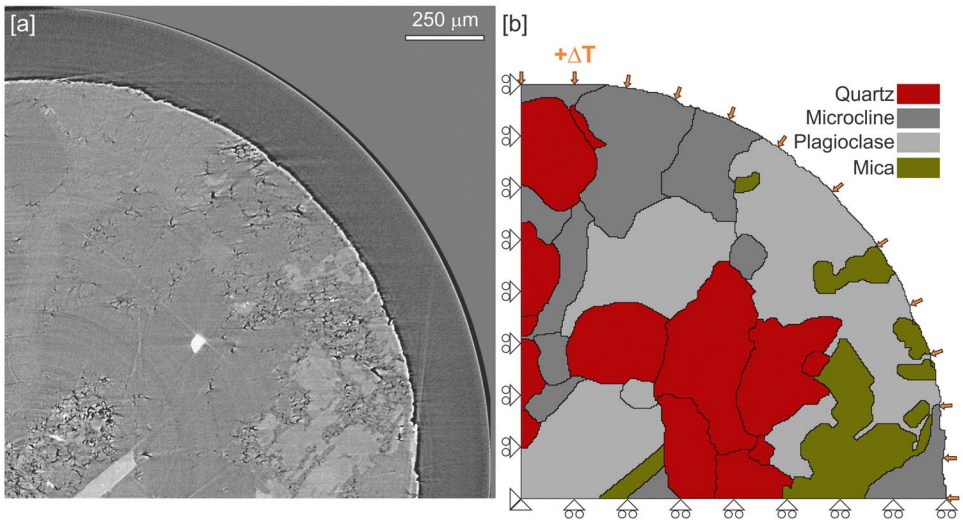


**Figure 2.** (a) Quarter of horizontal tomogram used fur numerical calibration (at 25°C) and (b) its simplified digital representation employed in our 2D FE simulations. The colors represent the different mineral phases (see legend), and the symbols denote the boundary conditions applied in the calibration step. Note the abundant pre-existing intracrystalline void space (black and dark gray colors, see for example, large plagioclase grain in lower left corner) and some cracked grain boundaries (for example, large quartz grain in upper left corner).

particularly affect the effective elastic moduli and thermal expansivities of minerals and rocks [*Bruner*, 1979, 1984; *Heard and Page*, 1982; *Rosen and Hashin*, 1970]. Therefore, we used results of our physical heating experiment on Westerly granite for empirical estimations of (a) the thermal expansivities of quartz, plagioclase, microcline, and mica, and (b) the yield strength and separation behavior of grain boundaries. This calibration step is described in the chapter at hand in the following order: (1) description of the physical heating experiment, (2) explanation of the numerical modeling approach, and (3) elucidation of the empirical calibration procedure.

## 3.1. The Physical Heating Experiment

[6] The heating experiment on Westerly granite was observed with high-resolution Synchrotron X-radiation microtomography at the bending magnet beamline (2-BM) of the Advanced Photon Source, Argonne National Laboratory, Chicago, USA. A cylindrical sample with a diameter of 2.5 mm and a height of 8 mm was glued to a sample mount at its base and heated in an X-ray transparent oven from 25°C to 220°C under atmospheric pressure with a temperature stepping scheme. In the first time step, the sample was heated to 50°C over a time interval of 2 min, then rested at this temperature for 10 min, and finally scanned. In all subsequent time steps, temperature was increased linearly by 10°C over a time interval of 10 min. This low heating rate guaranteed that no thermal cracking occurred due to a large spatial temperature gradient [*Richter and Simmons*, 1974]. After each heating step, the sample rested for 10 min before scanning commenced. Each scan took 25 min. A Si(111) monochromator provided 26-keV X-rays. Images were collected in transmission mode by a charge-coupled-device camera positioned behind the sample in the hutch configuration with an acquisition time of 200 ms. Data were collected through rotating the samples in 0.25° steps over 180°. Due to technical restrictions, only the central segment of the sample (length ~ 2.7 mm) was scanned. The minimum effective pixel size achieved is 1.3 micron. The output data were converted to stacks of grayscale TIFF images of size 2048 × 2048 pixel. The gray values are inversely proportional to the degree of X-ray absorption and thus permit identification of mineral phases, pores, and cracks (Figures 1a, 1b, and 2a). The detailed microstructural evolution of thermally induced void space in the granite sample will be presented in a separate paper. Here, we solely use the physical experiment to estimate poorly constrained material properties of the sample, as described below.

## 3.2. 2D Numerical Calibration Experiments: Methods

[7] For all 2D numerical simulations in this work, we used the commercial finite-element (FE) code Abaqus Standard [*Hibbit, Karlsson and Sorenson*, 2009], version 6.9 EF1. Abaqus Standard is a Lagrangian code employing implicit integration with

an adaptive time stepping scheme [e.g., *Regenauer-Lieb and Yuen*, 2004]. The thermal-loading problem was solved with coupled temperature-displacement analysis and the large-displacement formulation, which uses additive strain rate decomposition and Jaumann's stress rate [*Jaumann*, 1911]. The model features a simplified representation of the natural microstructure of the granite sample, obtained by manual digitization of a quarter of a tomogram cutting the cylindrical sample horizontally in its center (Figure 2), thus approximating plane-strain conditions. 87280 4-node bilinear first-order quadrilateral plane-strain elements (CPE4T) of edge length 3.765 micron were used. Model radius is 1.25 mm. Each grain boundary in the FE mesh served as contact surface. Hence, our numerical model combines aspects of FE and discrete-element method [*Karrech et al.*, 2008; *Zang*, 1993]: grains are modeled as discrete deformable bodies subject to contact interactions including grain-boundary cracking.

### 3.2.1. The Governing Equations

[8] Conservation of energy in Lagrangian notation and neglecting shear heating and possible source terms such as radioactive heat production is given by [*Regenauer-Lieb and Yuen*, 2003]

$$\rho c_p \frac{DT}{Dt} - \nabla(\kappa \nabla T) = 0, \tag{1}$$

where $\rho$ is density; $c_p$ is specific heat capacity; $T$ is temperature; $\frac{D(\cdot)}{D(\cdot)}$ is the material derivative; $t$ is time; and $\kappa$ is thermal conductivity. The conservation of mass is

$$\frac{D\rho}{Dt} + \rho \nabla \mathbf{v} = 0, \tag{2}$$

with $\mathbf{v}$ denoting the velocity vector. For quasistatic processes, the conservation of linear momentum is

$$\nabla \cdot \boldsymbol{\sigma} + \rho \mathbf{f} = 0, \tag{3}$$

where $\boldsymbol{\sigma}$ is the Cauchy stress tensor and $\mathbf{f}$ is the body force vector. The conservation of angular momentum ensures that $\boldsymbol{\sigma}$ is symmetric.

### 3.2.2. Rheology

#### 3.2.2.1. Grains

[9] In the calibration experiment, we used a linear-elastic, isotropic, homogeneous rheology for the grains:

$$\boldsymbol{\sigma} = \mathbf{c} : (\boldsymbol{\varepsilon} - \boldsymbol{\varepsilon}_\mathbf{T}), \tag{4}$$

with $\mathbf{c}$ being the fourth-order stiffness tensor, $\boldsymbol{\varepsilon}$ is the second-order total strain tensor, and $\boldsymbol{\varepsilon}_\mathbf{T}$ is the second-order thermal strain tensor. In case of isotropic behavior, equation (4) can be written as $\boldsymbol{\sigma} = \left(K - \frac{2}{3}G\right) tr(\varepsilon)\mathbf{1} + 2G\varepsilon - 3\alpha K(T - T_0)\mathbf{1}$, where $K$ is bulk modulus (the inverse of compressibility), $G$ is shear modulus, $\alpha$ is linear thermal expansivity, and $\Delta T = (T - T_0)$ is the temperature change. Therefore, thermal expansion and compressibility affect the mean stress (the isotropic part of $\boldsymbol{\sigma}$) as follows: $\frac{\boldsymbol{\sigma_{ii}}}{3} = 3K\frac{\boldsymbol{\varepsilon_{ii}}}{3} - 3\alpha K \Delta T$, where $\frac{\boldsymbol{\varepsilon_{ii}}}{3}$ is the isotropic part of the total strain tensor. A purely elastic rheology is justified because, under the conditions of the physical experiment, ductile creep in feldspar and quartz are negligible. Mica might deform plastically under these conditions. However, we neglected this because mica is a minor component in the slice considered (11%). Yet energy dissipation by grain-boundary cracking was considered, as explained in the next section.

#### 3.2.2.2. Grain Boundaries

[10] In both the 2D calibration and burial models, grain boundaries were simulated as contact surfaces using the node-to-surface contact method with a master-slave approach [*Hibbit, Karlsson and Sorenson*, 2009]. We found that shear displacements between grains are negligible in our experiments. Hence, small-sliding tracking was employed and interface friction neglected; thereby, computation time was decreased. In compression, the stiffness of the contact surface is determined by the material properties of the enclosed grain. In tension and shear, contact surfaces obey an empirical elastoplastic damage law (Figure 3):

$$\tau(d) = \begin{cases} d \le d_{crit} \rightarrow \tau(d) = K_n d \\ d < d_{crit} \rightarrow \tau(d) = \tau_Y(1 - D(d)) \end{cases}, \tag{5}$$

where $\tau$ is tensile/shear traction; $\tau_y$ is tensile/shear yield stress; $d$ is extensional/shear displacement; $K_n$ is an elastic modulus; and $D$ is a damage parameter assuming values between 0 and 1. This law is formulated as a function of $d$. Below a critical displacement $d_{crit}$, the surface behaves linear-elastically. If displacement exceeds $d_{crit}$, the critical yield stress is reached and irreversible grain-boundary damage occurs. With ongoing displacement, tractions on the grain boundary decay exponentially until a maximum displacement $d_{\max}$, beyond which no tensile or shear tractions are transmitted. At this point, the grain

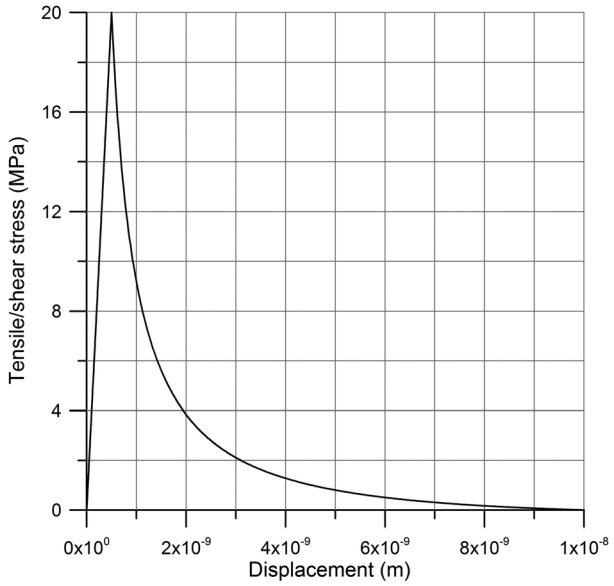


**Figure 3.** Plot of rheological damage law used for grain boundaries in tension and shear.

boundary segment is completely cracked and cohesionless. The exponential decay is contained in the damage parameter $D$ [*Hibbit, Karlsson and Sorenson*, 2009]:

$$D(d) = 1 - \frac{d_{crit}}{d}\left(1 - \frac{1 - \exp\left(\frac{-a(d - d_{crit})}{d_{\max} - d_{crit}}\right)}{1 - \exp(-a)}\right), \quad (6)$$

where $a$ is a shape parameter. Healing of cracked grain boundaries was not considered and not expected on the time scale of the physical experiment. However, if cracked grain boundaries come in contact again at a later stage, compressive stresses are transmitted.

### 3.2.3. Boundary and Initial Conditions

[11] For the sake of computational speed, we considered a quarter cylinder of Westerly granite (Figure 2). Nodes on the straight radial edges could only move in the respective radial direction while the node at the origin of the quarter cylinder remained fixed (Figure 2b). Temperature boundary conditions were applied to all nodes on the outer arc, in accordance with the heating scheme employed in the physical experiment. Initial temperature was 25°C everywhere in the model. 60% of all grain boundaries were cracked prior to heating in accordance with microstructural investigations of Westerly granite [*Moore and Lockner*, 1995]. Cracked grain-boundary segments were chosen with a random algorithm. Crack widths were also assigned randomly, according to a Gaussian distribution with a mean of 0.5 micron and lower and upper bounds of 0.1 and 1.0 micron, respectively.

### 3.2.4. Material Properties of Undamaged Minerals

#### 3.2.4.1. Grains

[12] We used temperature-dependent thermal expansivities, elastic moduli, and specific heat capacities for the undamaged minerals (Figure 4). For the calculation of thermal expansivities, we used data from the experimental literature (Figure 5, quartz: *Ackermann and Sorrell* [1974], feldspars: *Skinner* [1966], and mica: *Chon et al.* [2003]). These papers permit the computation of strain-temperature curves for the respective crystallographic axes of the mineral of interest. Linear thermal expansivities for all principal axes were calculated as secant slopes of the strain-temperature curves (i.e., with respect to the initial temperature, not as local derivative) and averaged (Figure 5). Temperature-dependent elastic moduli and specific heat capacities were calculated with the Gibbs energy minimizer Perplex [*Connolly*, 2005]. This method yielded problematic results for mica. For the elastic parameters of mica, we thus resorted to experimental data that do not consider temperature dependence [*Bass*, 1995]. This is justified because of the small proportion of mica in the sample and the fact that elastic properties of minerals generally experience smaller changes over the regarded temperature interval than thermal-expansion properties (Figure 4). Specific heat capacity (Figure 4b) of undamaged mica changes significantly over the considered temperature interval and was taken from the literature [*Berman*, 1988]. Mineral densities and thermal conductivities and their sources are listed in Table 1.

#### 3.2.4.2. Grain Boundaries

[13] For simplicity, we applied the same contact properties to all grain boundaries. Parameter sensitivity studies of the grain-boundary law showed that tensile yield strength is the most relevant parameter for grain-boundary separation behavior (Figure 6). This is consistent with the notion that grain boundary cracks generally propagate in a tensile fashion [*Kranz*, 1983]. Within a physically reasonable parameter space, the model is insensitive to choices of $d_{crit}$, $d_{\max}$, and shear behavior.

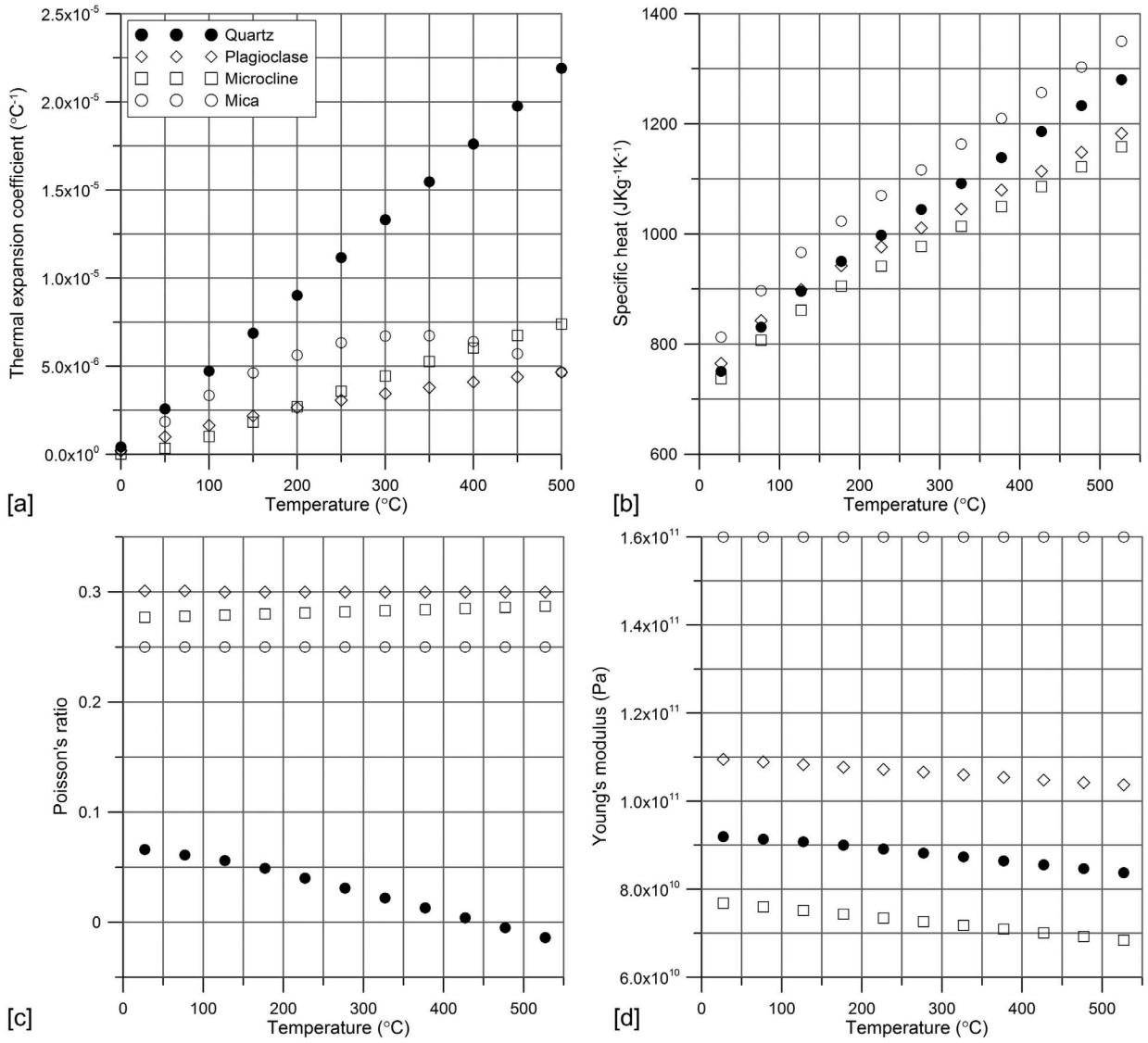


**Figure 4.** Plots of temperature-dependent thermal-elastic material properties used in the 2D simulations. They were implemented as look-up tables as shown here. Abaqus interpolates linearly between points. (a) Downscaled mean effective thermal expansion coefficients obtained from calibration. For literature data for undamaged minerals, see Figure 5. (b) Specific heat, calculated with Gibbs energy minimizer Perplex [*Connolly*, 2005]. Data for mica are computed after *Berman* [1988]. (c) Poisson's ratio, calculated with Perplex [*Connolly*, 2005]. Data for mica are from *Bass* [1995]. (d) Young's modulus, calculated with Perplex. Data for mica are from *Bass* [1995].

Therefore, shear behavior was assigned the same parameters as tensile behavior. $d_{crit}$ and $d_{\max}$ were estimated from theoretical work on tensile behavior of quartz grain boundaries based on atomic binding models [*Tromans and Meech*, 2004]. It is expected that the tensile yield strength of the grain boundaries is close to the tensile strength of the aggregate [*Tromans and Meech*, 2004]. For our Westerly granite sample, we used the experimentally determined value of 20 MPa [*Moore and Lockner*, 1995]. When grain boundaries are cracked, heat flux $q$ per unit surface area is calculated with a radiation law [*Hibbit, Karlsson and Sorenson*, 2009]:

$$q = H\left[(T_A - T_0)^4 - (T_B - T_0)^4\right], \tag{7}$$

where $T_A$ and $T_B$ denote the temperatures of the adjacent cracked grain surfaces, $T_0$ is the absolute zero on the employed temperature scale, and $H$ is a coefficient determined by

$$H = \frac{F\zeta}{\frac{1}{e_A} + \frac{1}{e_B} - 1}, \tag{8}$$

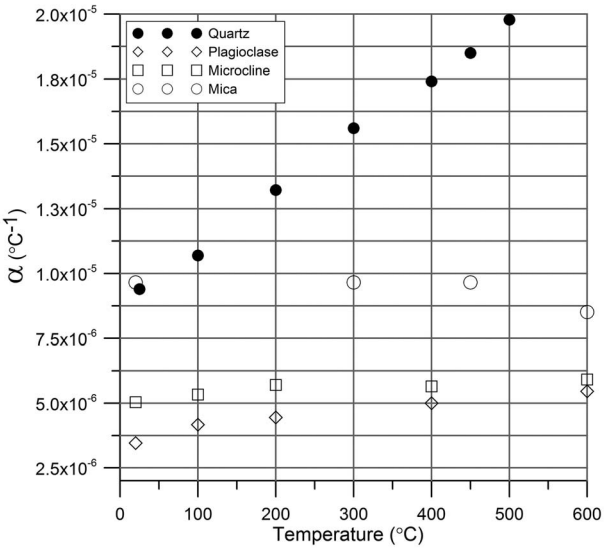


**Figure 5.** Mean effective thermal expansivities for quartz, plagioclase, microcline, and mica determined from laboratory experiments. Data are from *Ackermann and Sorrell* [1974] for quartz; *Chon et al.* [2003] for mica; and *Skinner* [1966] for microcline and plagioclase.

where $\zeta$ is the Stefan-Boltzmann constant, $F$ is the effective view factor, and $e_A$ and $e_B$ are the emissivities of the adjacent grain surfaces. When grain boundaries are closed, heat is transferred conductively:

$$q = K(T_A - T_B), \tag{9}$$

where $K$ denotes the grain boundary conductance. When grain boundaries start to separate, $K$ decreases linearly as a function of normal distance between adjacent grain boundaries and assumes a value of 0 once a distance of $1.0 \times 10^{-10}$ m has been reached. The values of all grain-boundary material parameters are summarized in Table 2.

## 3.3. Calibration of the 2D Numerical Experiment

[14] Our numerical approach cannot simulate pre-existing intracrystalline micro-damage explicitly, for example, the abundant pores in plagioclase and intragranular and transgranular cracks (Figures 1a, 1b, and 2a). Both intracrystalline and intercrystalline void space may locally accommodate thermal expansion of minerals [*Cooper and Simmons*, 1977; *Darot et al.*, 1992]. As a result, the bulk thermal expansivity of an unconfined rock sample can be smaller at low temperatures than that predicted from the thermal expansivities of its mineralic components assuming they were intact [*Cooper and Simmons*, 1977]. Previously reported permeability measurements on thermally treated granite show a minimum in the temperature interval 20–125°C, also attributed to the closure of pre-existing void space [*Darot et al.*, 1992]. Using the thermal expansivities for the undamaged minerals without pre-existing open grain-boundary cracks in the numerical model leads to a significant overestimation of the mean radial displacement observed in the physical experiment (Figure 7a). Including 60% pre-existing open grain boundaries in the simulation improves the results somewhat but still yields an overestimation of final displacement by a factor of 3 (Figure 7a). We attribute this discrepancy to (a) the considerable amount of pre-existing intracrystalline damage observed in our sample (Figures 1 and 2), (b) the fact that the pre-existing open model grain boundaries were chosen randomly, and (c) the reduced spatial dimensionality of our model (2D versus 3D). In order to account for this discrepancy, we regarded the thermal expansivities of our damaged mineral phases as free fitting parameters and reduced them empirically until our numerical experiment matched the radial deformation history of the physical experiment (see below). Intracrystalline damage also lowers the elastic moduli of the affected minerals and thereby internal stresses [*Heard and Page*, 1982; *Nasseri et al.*, 2009]. However, we lumped this effect solely into the downscaling of thermal expansivities for two reasons: first, *Bruner* [1984] demonstrated that, in quartzo-feldspathic rocks, thermal-expansion mismatch makes the main contribution to internal stresses for geologically reasonable geotherms; second, the degrees of freedom in the numerical calibration are reduced.

[15] For calibration, we selected a horizontal tomogram in the center of the sample cylinder to approximate plane-strain conditions (Figure 2a). Mean radial displacement and mean radial strain evolution for this tomogram were determined as follows. The grayscale tomogram, obtained at a given temperature, was first converted into a binary

**Table 1.** Mineral Densities, $\rho$, and Conductivities, $K$, Used in the 2D Models

| Mineral | $\rho$ (kgm$^{-3}$) | $K$ (Wm$^{-1}$K$^{-1}$) |
|---|---|---|
| Quartz | 2624.31[a] | 6.15 |
| Plagioclase | 2756.50[a] | 2.72 |
| Microcline | 2555.30[a] | 2.34 |
| Mica | 2844.00[b] | 3.14 |

[a]Calculated with Perplex [*Connolly*, 2005].
[b]From *Bass* [1995]. Conductivities taken from *Clauser and Huenges* [1995].

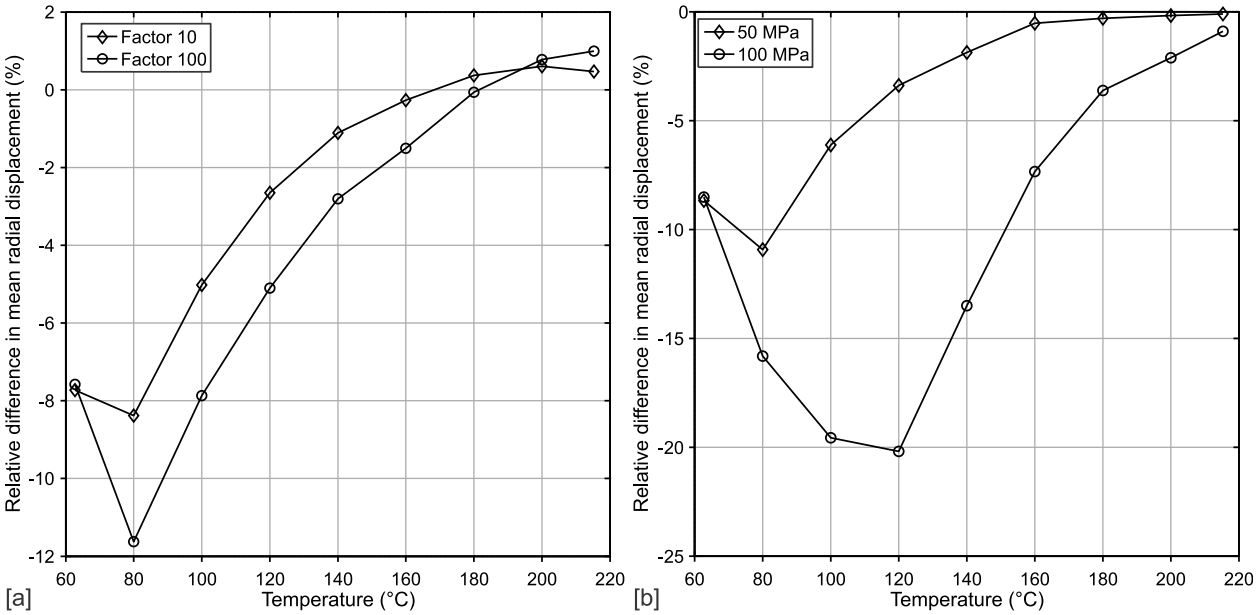


**Figure 6.** Sensitivity of 2D calibration model to grain-boundary rheology, namely choices of (a) $d_{crit}$ and $d_{\max}$, and (b) yield strength. Sensitivity tests were run for simulations in which all grain boundaries were closed prior to heating. Vertical axes show the difference in mean radial displacements between sensitivity-test and successful calibration model normalized by the results of the calibration model. Even an unreasonably high increase of $d_{crit}$ and $d_{\max}$ by a factor of 100 (circles in Figure 6a) results in a maximum decrease of mean radial displacement by less than 12%. The results are more sensitive to the choice of yield strength. An increase of yield strength from the used 20 MPa to 100 MPa (factor of 5, circles in Figure 6b) results in a maximum difference in mean radial displacement of 20%.

image via binary thresholding, where pixels belonging to the rock sample assume a value of 1, while those making up the sample surrounding are assigned a value of 0. This was possible with great accuracy because the sample is surrounded by air, which has a significantly lower X-ray absorption than the rock sample (Figure 2a). In the next step, the centroid of the circular sample region was calculated. The set of sample radii, for each temperature step, is given by the Euclidian distances between the centroid and each pixel at the sample perimeter. Finally, the mean of the set of radii was determined for each temperature step. Radial strain $\varepsilon_R$ was then computed as

$$\varepsilon_R(t_i) = \frac{r(t_i) - r(t_0)}{r(t_0)}, \tag{10}$$

where $r(t_i)$ is mean radius at time $i$, and $r(t_0)$ is mean radius prior to heating. Linear thermal expansivity at time $i$ was obtained by dividing $\varepsilon_R(t_i)$ by the temperature difference accrued over the time interval $t_i - t_0$. The same measurement procedure was applied to evaluate the numerical experiments. Despite the high resolution of our tomograms, the signal-to-noise ratio is small, resulting in considerable uncertainty of our radial displacement and strain measurements (Figures 7a and 7b). The sample margin can be resolved to within +/−1 pixel (i.e., +/−1.3 micron). However, total radial displacements range from 3 to 5 pixel. Hence, the strain error is of order of $+/-2.3 \times 10^{-3}$.

[16] We used the following empirical tuning procedure to match the numerical to the physical results. A certain constant value was subtracted from the mean thermal expansivity of undamaged quartz at the temperature of 0°C. A different constant value was then subtracted from the mean thermal expansivity of undamaged quartz at the temperature of

**Table 2.** Grain Boundary Properties

| $\tau_y$ (MPa) | $d_{crit}$ (m) | $d_{\max}$ (m) | $a$ | $K_n$ ($m^{-1}$MPa) | $\zeta$ ($Wm^{-2}K^{-4}$) | $F$ | $e_A$, $e_B$ | $K$ ($JK^{-1}m^{-2}s^{-1}$) |
|---|---|---|---|---|---|---|---|---|
| 20 | $5.0 \times 10^{-10}$ | $1.0 \times 10^{-8}$ | 1 | $4.0 \times 10^{10}$ | $5.67 \times 10^{-8}$ | 1 | 0.8 | 1000.0 |

500°C. The subtrahends for all thermal-expansion values within this temperature interval were simply determined by linear interpolation between the initial and final subtrahends. Changing subtrahends were used because the discrepancy of the displacement predictions is largest at low temperatures (overestimation by about a factor of 8) and smallest at high temperatures (overestimation by about a factor of 3) (Figure 7a). The mean thermal expansivities of the other minerals were then scaled such that their ratios to those of tuned quartz remained equal to the ratios of their undamaged expansivities to those of undamaged quartz. Of course there are various physically more reasonable homogenization procedures for the determination of effective properties from tomography data [e.g., *Hashin and Shtrikman*, 1963; *Knackstedt et al.*, 2006; *Rosen and Hashin*, 1970; *Walsh*, 1973]. However, these techniques require the geometrical characterization of intracrystalline void space for each mineral phase as a function of temperature. For the tomography data used here, this would present an extremely laborious task. The segmentation of single mineral grains would have to be done manually because (a) grain boundaries are often at the resolution limit, and (b) the gray-value histograms of quartz and plagioclase overlap to a great degree, thus rendering automated segmentation methods challenging. Moreover, image noise is significant and artifacts fairly common (Figure 2a), hampering automated segmentation of intracrystalline voids and leading to errors in porosity measurements. However, a new series of heating experiments features substantial technical improvements. Our new 4D data will be used with more sophisticated approaches to material characterization in the near future.

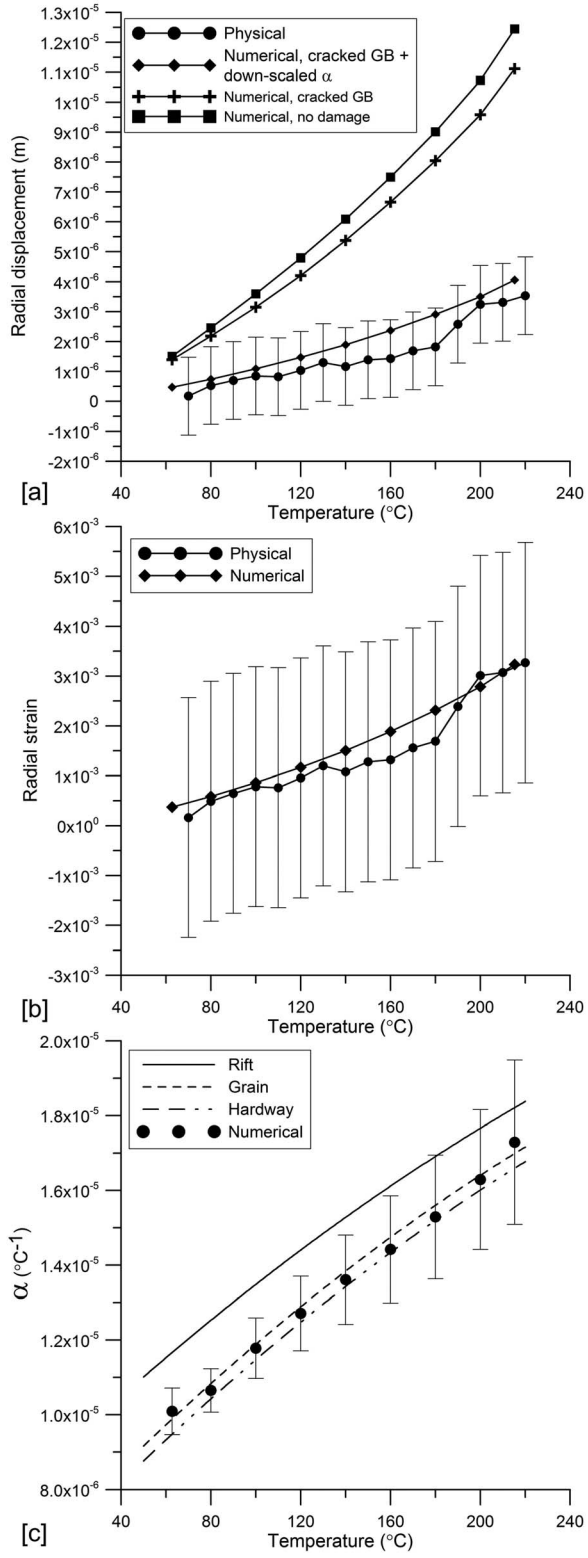


**Figure 7.** Results of numerical calibration. (a) Comparison of mean radial displacement for physical experiment (circles) and calibrated numerical model (diamonds). Error bars on the physical data are for an accuracy of +/−1 pixel. Square symbols denote radial displacement history for a simulation using mean linear expansion coefficients for intact minerals and disregarding pre-existing grain-boundary cracks. Cross symbols represent results for a model that involves 60% pre-cracked grain boundaries but without down-scaling of mean linear expansion coefficients. For explanation, see text. (b) Mean radial strain in physical and calibrated numerical experiment. Error bars on physical data are calculated with linear error propagation assuming a displacement error of +/−1 pixel. (c) Linear thermal expansivities from experiments of *Cooper and Simmons* [1977] versus mean linear expansivity predicted by our calibrated model. The terms 'rift', 'grain', and 'hardway' are quarrying terms denoting planes of easiest, intermediate, and hardest splitting of the rock. *Cooper and Simmons* [1977] cut their samples accordingly and measured linear expansivities normal to these planes. Error bars on numerical data indicate the standard deviation of the mean linear expansivities measured for all nodes on the arc of quarter cylinder.

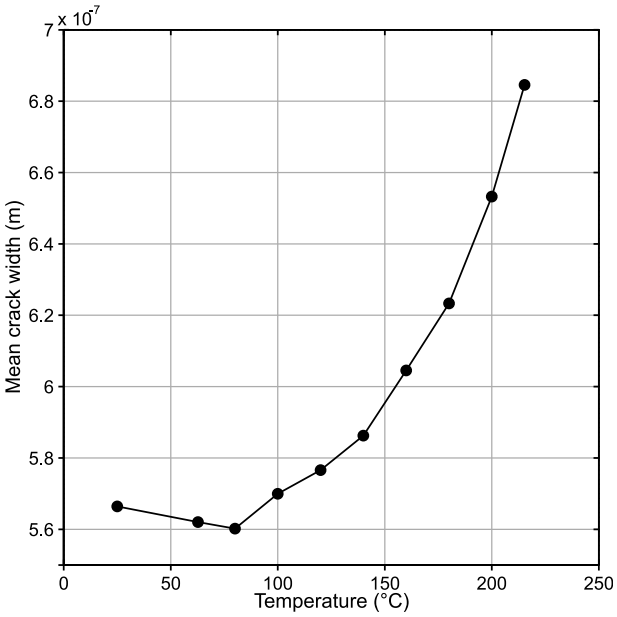


**Figure 8.** Plot of mean width of all grain boundary cracks over temperature observed in the calibrated 2D heating model. The minimum at 80°C indicates closure of pre-existing grain boundary cracks, as predicted previously [e.g., *Cooper and Simmons*, 1977; *Darot et al.*, 1992]. Observed crack width is of the same order as that measured in previous laboratory experiments on Westerly granite [*Nasseri et al.*, 2007].

[17] Using a low-temperature subtrahend of $6 \times 10^{-6}$ K$^{-1}$ (a reduction of the mean linear expansivity of undamaged quartz at 0°C by ~71%) and a high-temperature subtrahend of $10^{-5}$ K$^{-1}$ (a reduction of the mean linear expansivity of undamaged quartz at 500°C by ~33%), we obtained a satisfactory fit to the radial displacement and strain history of our physical experiment (Figures 7a and 7b). Because measurement uncertainty in our physical experiments is high, we also compared the numerical results to data reported in the literature: the evolution of bulk linear thermal expansivity as a function of temperature [*Cooper and Simmons*, 1977]. Our tuned model predicts the literature data excellently (Figure 7c). In accordance with laboratory experiments [*Cooper and Simmons*, 1977; *Darot et al.*, 1992], the fitted numerical model also predicts closure of pre-existing grain-boundary cracks in the low-temperature regime (Figure 8).

## 4. 1D Calculations

[18] Before we extend the calibrated 2D simulations to the modeling of burial-induced grain-scale thermal-elastic stresses in a viscoelastic medium, we present simple, instructive 1D calculations that illustrate the first-order physics of this problem.

### 4.1. Methods

[19] Consider a volume element of rock that is heated as it moves from the Earth's surface into the crust with constant velocity along a simple equilibrium geotherm with a temperature of 0°C at the Earth's surface and constant surface heat flux [*Fowler*, 1990]. The heating rate depends on the geotherm and the burial velocity, $v$, and can be obtained by differentiation of the heating function (i.e., the geotherm):

$$T(t) = \frac{-H(z_0 + vt)^2}{2\kappa} + \frac{Q_0(z_0 + vt)}{\kappa} + T_s, \qquad (11)$$

Where $T$ is temperature; $T_s$ is temperature at the surface; $H$ is heat production of continental crust; $\kappa$ is thermal conductivity of the crust; $Q_0$ is surface heat flux; $z_0$ is initial depth (see Table 3 for parameters used here). To isolate thermal effects, we neglect tectonic background deformation and confining pressure. For the rheology of the rock element, we adopt a viscoelastic model, combining a linear-elastic spring with a nonlinear dashpot in series. Thus, the total strain rate $\dot{\varepsilon}$ is the sum of elastic and viscous strain rates:

$$\dot{\varepsilon} = \dot{\varepsilon}_{EL} + \dot{\varepsilon}_V, \qquad (12)$$

where subscripts '*EL*' and '*V*' denote 'elastic' and 'viscous', respectively. Dots indicate time derivatives, here of strain, $\varepsilon$. In the 1D case, the elastic strain rate reads

$$\dot{\varepsilon}_{EL} = \frac{1}{E}\dot{\sigma}, \qquad (13)$$

where $E$ is Young's modulus and $\sigma$ is stress. For the viscous strain rate, we employ the commonly used power-law flow law [e.g., *Buergmann and Dresen*, 2008]:

$$\dot{\varepsilon}_V = A\sigma^n f_{H_2O}^r \exp\left(\frac{-Q}{RT(t)}\right), \qquad (14)$$

where $A$ is a pre-exponential constant, $n$ is the power-law exponent, $f_{H_2O}$ is water fugacity with exponent $r$, $Q$ is activation energy, and $R$ is the gas

**Table 3.** Parameters Used for Calculation of Equilibrium Geotherm[a]

| $H$ (Wm$^{-3}$) | $K$ (Wm$^{-1}$K$^{-1}$) | $Q_0$ (mWm$^{-2}$) |
|---|---|---|
| $1.0 \times 10^{-6}$ | 3.0 | 60, 70, 80, 90 |

[a] $H$ is heat production, $K$ is conductivity, and $Q_0$ is surface heat flow.

**Table 4.** Parameters for Power Law Flow[a]

| Mineral | Log($A$) (MPa$^{-n}$micron$^{m}$s$^{-1}$) | $n$ | $Q$ (KJmol$^{-1}$) | $r$ | $f_{H_2O}$ (MPa) |
|---|---|---|---|---|---|
| Quartz [*Rutter and Brodie*, 2004] | −4.93 | 2.97 | 242 | 1 | 300 |
| Quartz [*Hirth et al.*, 2001] | −11.20 | 4.00 | 135 | 1 | 37 |
| Feldspars [*Rybacki and Dresen*, 2000] | 2.60 | 3.00 | 356 | 0 | 1 |
| Mica [*Kronenberg et al.*, 1990] | −29.92 | 18.00 | 51 | 0 | 1 |

[a]$A$ is a pre-exponential constant, $n$ is the power law exponent, $Q$ is activation energy, $r$ is a fugacity exponent, and $f_{H2O}$ is water fugacity.

constant. The parameters used in this study are listed in Table 4. We consider thermal expansion mismatch as the only source for internal stresses in the 1D case. Neglected sources for thermal-elastic stresses are the anisotropies of the thermal expansion tensors and the different elasticity tensors of the minerals [*Evans*, 1978; *Skinner*, 1966]. These sources induce internal stresses in buried monomineralic rocks and lead to a greater range in magnitudes of thermal-elastic stresses in polyphase rocks. However, they are ignored here because the large difference of thermal expansivity between quartz and feldspar is the main source of internal stresses in granitic rocks [*Bruner*, 1984]. To simulate thermal expansion mismatch in 1D, we employed the temperature-dependent difference of the mean effective expansivities, $\Delta\bar{\alpha}(t)$, of quartz and a respective partner mineral (feldspars or mica), as derived from our 2D calibration experiment. $\Delta\bar{\alpha}(t)$ was calculated from the data of our calibration experiment (Figure 4a) and fitted with a second-order polynomial: $\Delta\bar{\alpha}(t) = pT(t)^2 + qT(t) + \alpha_0$ (see Table 5 for parameters). The total strain rate applied to the 1D viscoelastic element is simply the product of the heating rate and $\Delta\bar{\alpha}(t)$:

$$\dot{\varepsilon} = \Delta\overline{\alpha}(t)\dot{T}(t) = \left(pT(t)^2 + qT(t) + \alpha_0\right) \cdot \left[\frac{v}{\kappa}(Q_0 - H(z_0 + vt))\right]. \quad (15)$$

Combining equations (12)–(15) and rearranging yield the nonlinear ordinary differential equation:

$$\dot{\sigma} = E\left[\Delta\overline{\alpha}(t)\dot{T}(t) - \sigma^n A f_{H_2O}^r \exp\left(\frac{-Q}{RT(t)}\right)\right]. \quad (16)$$

Integration of equation (16) gives the desired viscoelastic stress evolution. Analytical solutions can be derived for power-law exponents of 1, 2, and 3 or zero strain rate. However, we also used flow laws with different exponents (Table 4). Therefore, equation (16) is integrated numerically with the explicit fourth-order Runge-Kutta method.

## 4.2. Results

[20] We explored typical geotherms and burial velocities encountered in nature. The considered geothermal gradients are well above the critical gradient at which compressibility cancels thermal expansion [*Bruner*, 1984]. Figures 9a and 9b show typical curves for thermal-elastic stress versus depth for quartz and plagioclase. The elastic stress response is nonlinear because of the temperature dependence of thermal expansivity. The curves reach a marked maximum beyond which accelerated viscous creep relaxes thermal-elastic stresses exponentially. The stress maximum is of particular interest. It marks the onset of effective viscous relaxation, i.e., viscous stress relaxation rate exceeding elastic-stress build-up rate. As expected for our rheological model, the magnitude of the peak stress increases with increasing burial velocity and only slightly for hotter geotherms (Figure 10, top row). It ranges from 120 to 200 MPa in wet quartz [*Rutter and Brodie*, 2004], and from 250 to 367 MPa in wet anorthite [*Rybacki and Dresen*, 2000]. Temperature at peak stress increases strongly with burial velocity and gently for hotter geotherms (Figure 10, middle row). It ranges from 300 to 380°C for wet quartz, and from 388 to 465°C for wet anorthite. The relaxation time (in the 1D case, the ratio of the material's effective viscosity over its Young's modulus) at peak stress decreases with increasing burial velocity and for hotter geotherms (Figure 10, bottom row). For wet quartz [*Rutter and Brodie*, 2004], it ranges from 48 Ma to 33 ka, and for wet anorthite [*Rybacki and Dresen*, 2000] from 75 Ma to 43 ka. Peak relaxation time

**Table 5.** Coefficients for Quadratic Fit to Temperature-Dependent Differences of Mean Effective Thermal Expansivity

| Mineral Pair | $p$ (K$^{-3}$) | $q$ (K$^{-2}$) | $\alpha_0$ (K$^{-1}$) |
|---|---|---|---|
| Quartz – Plagioclase | 1.0580e-011 | 2.3361e-008 | −7.0272e-006 |
| Quartz – Microcline | −1.986e-012 | 2.9368e-008 | −7.1802e-006 |
| Quartz – Mica | 6.2237e-011 | −3.1455e-008 | 4.2937e-006 |

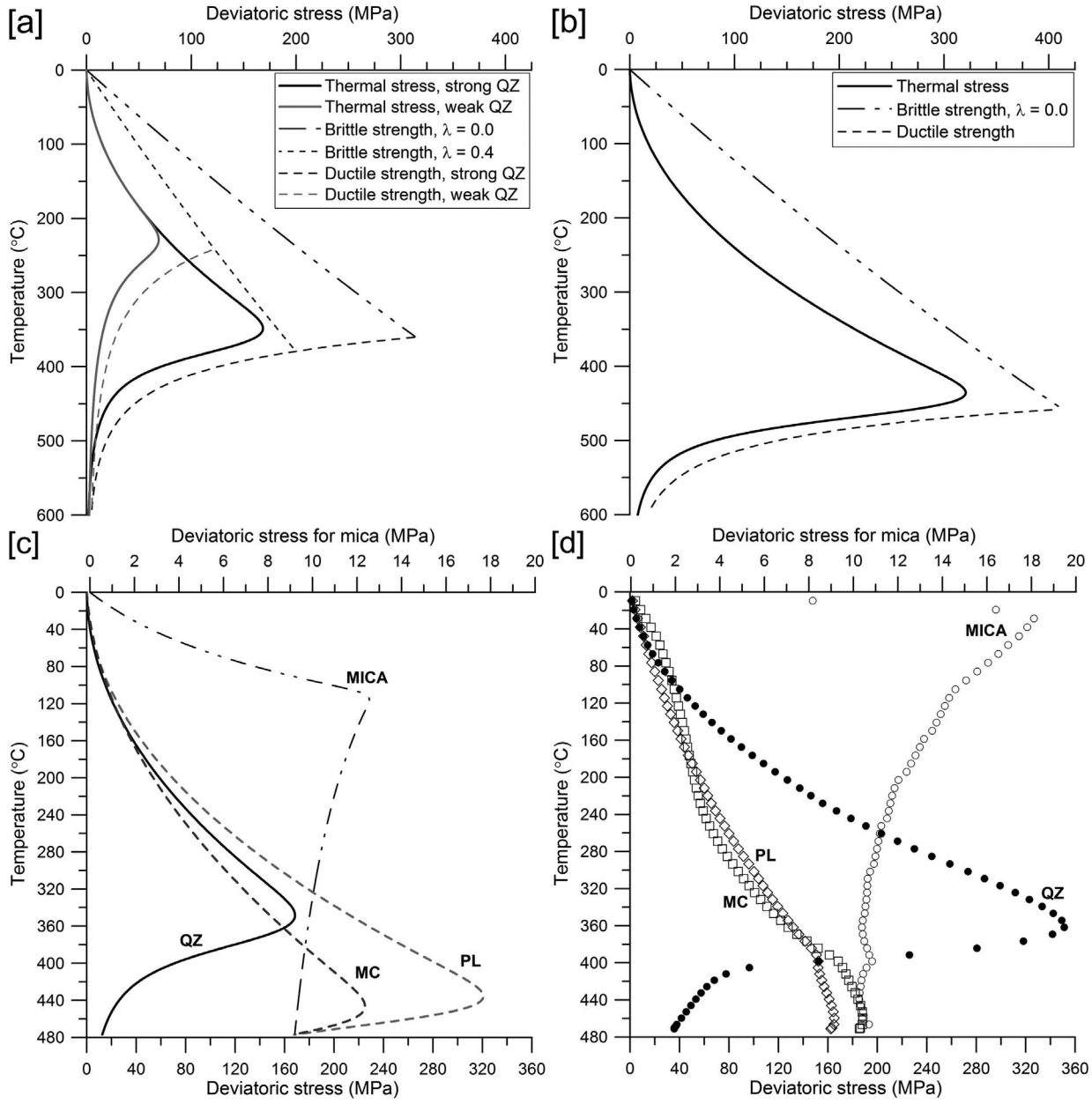


**Figure 9.** (top row) Results of 1D burial calculation for a burial velocity of 0.01 m/a, and a geotherm that corresponds to the global average surface heat flow of continental crust, 70 $mWm^{-2}$. (a) Thermal stress as a function of temperature for strong [*Rutter and Brodie*, 2004] (bold solid black curve) and weak [*Hirth et al.*, 2001] (bold solid gray curve) quartz. Dashed nonlinear curves indicate viscous strength for strong and wet quartz at a typical tectonic strain rate of $10^{-15}$ $s^{-1}$. Dashed linear curves denote brittle strength in tension for dry rock ($\lambda = 0$) and for rock with hydrostatic pore fluid pressure ($\lambda = 0.4$). In both cases, zero cohesion and a friction coefficient of 0.8 are used. (b) Thermal stress over temperature for plagioclase [*Rybacki and Dresen*, 2000] (bold black curve). Dashed lines give viscous strength (nonlinear curve) and brittle strength of dry rock ($\lambda = 0$) in tension. Strain rate, friction coefficient, and cohesion are the same as in Figure 9a. (bottom row) Comparison of 1D and 2D calculations. (c) 1D results: plots of deviatoric thermal stress over temperature for quartz (QZ; paired with plagioclase), plagioclase (PL; paired with quartz), microcline (MC; paired with quartz), and mica (MICA; paired with quartz). Note that mica curve relates to *x* axis on the top of the diagram, both in Figures 9c and 9d. A burial velocity of 0.01 m/a, and a geotherm according to a surface heat flow of 70 $mWm^{-2}$ are used. [d] 2D results: plots of mean deviatoric thermal stress for all four mineral phases. Data labels and burial conditions are the same as in Figure 9c.

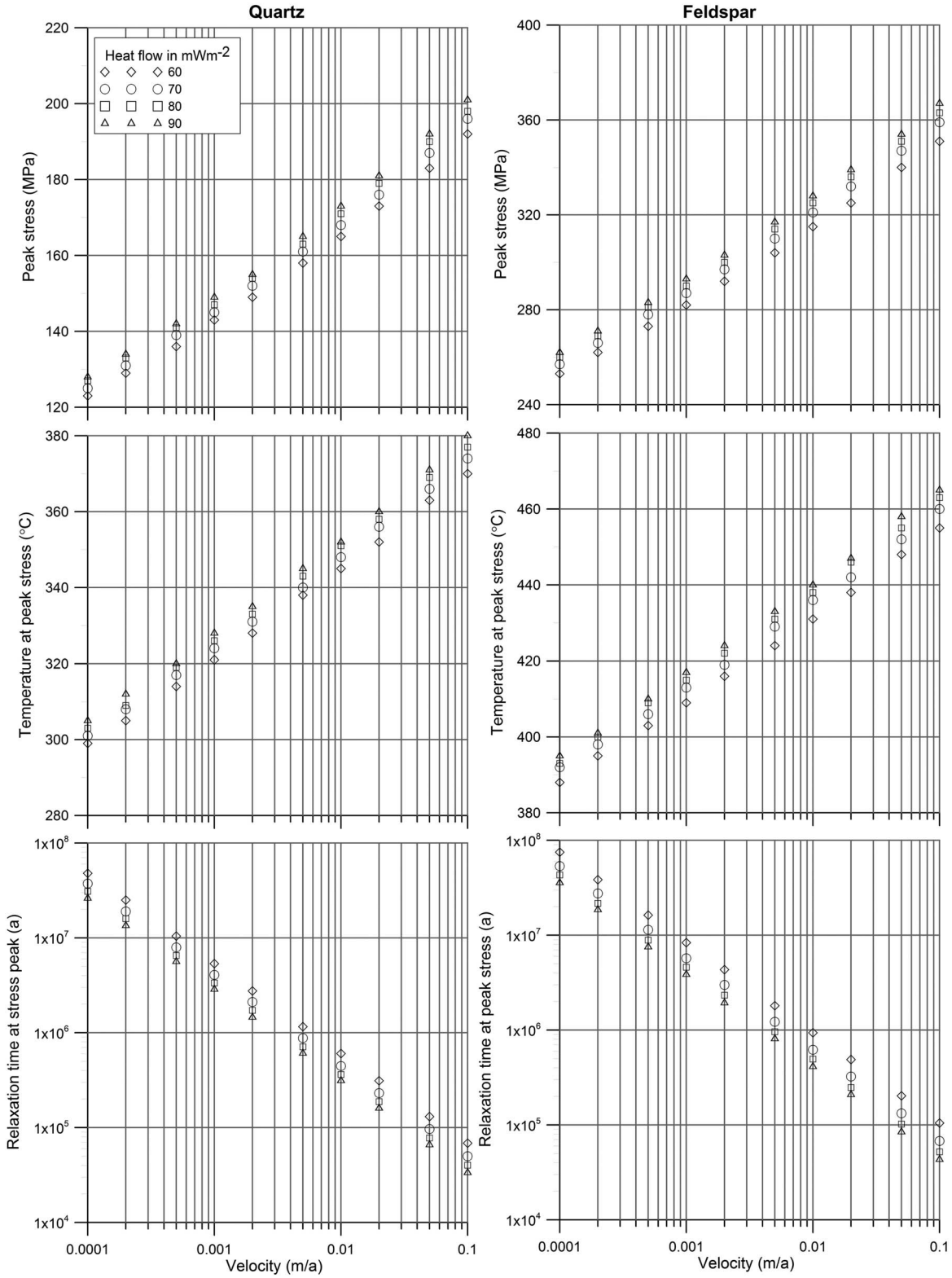


**Figure 10.** Results of 1D parameter study for (left column) quartz [*Rutter and Brodie*, 2004] and (right column) plagioclase [*Rybacki and Dresen*, 2000]. Plots provide results for four different heat flow values and ten burial velocities covering four orders of magnitude. (top row) Peak stress; (center row) temperature at peak stress; (bottom row) relaxation time at peak stress.

is <1 Ma for geologically high burial velocities ≥5 mm/a only. Values <100 ka occur only for very high velocities ≥5 cm/a. In summary, the 1D burial models imply that thermal-elastic stresses can reach magnitudes >100 MPa in dense quartz- and feldspar-rich rocks with relaxation times well above 100 ka.

[21] The most striking result is revealed if one plots classical Brace-Goetze strength profiles [*Brace and Kohlstedt*, 1980; *Goetze and Evans*, 1979] for continental crust into the same stress-temperature diagram (Figures 9a and 9b): deviatoric thermal-elastic stresses render the subsiding rock volume close to failure, both in the brittle and ductile regime. The thermal stress curve depends intimately on the applied flow law. Especially for quartz, there is a considerable spread of laboratory flow strengths, mainly due to its mechanical sensitivity to water content [*Blacic*, 1981; *Hirth et al.*, 2001; *Regenauer-Lieb*, 2006; *Rutter and Brodie*, 2004]. The flow laws used in Figure 9a bracket the range of existing flow laws for quartz [*Buergmann and Dresen*, 2008]. Regardless of the choice, the ductile strength envelope is also shifted according to the applied flow law. Hence, thermal-elastic stresses always contribute significantly to the overall deviatoric stress. This effect seems most pronounced at the brittle-ductile transition.

## 5. 2D Calculations of Burial-Induced Internal Stresses

[22] The 1D model involves three notable simplifying assumptions. First, deformation of the respective virtual partner mineral is neglected. However, the viscoelastic deformability of a mineral's neighbors in nature introduces further nonlinearity in its stress history. Second, microstructure is disregarded although it affects the internal stress field [*Bruner*, 1984; *Eberhardt et al.*, 1999]. Third, the 1D model ignores compressibility and confining pressure, i.e., mechanical loading. During burial, a rock experiences an increase in both pressure and temperature. Since the minerals in granite are compressible, the pressure increase leads to volume reduction. The temperature increase, in contrast, causes a counteracting volume expansion. The thermal effect dominates for realistic geothermal gradients and controls internal stresses [*Bruner*, 1984]. In order to better understand the combination of all three effects, we used our calibrated 2D FE models and applied them to the burial problem.

### 5.1. Methods

[23] Key differences to the 1D model include: (1) the 2D burial model employs real microstructure of Westerly granite digitized from a 2D tomogram; (2) it contains the four phases quartz, plagioclase, microcline, and mica (Figure 2), hence the mismatch of their elastic properties is also considered in the internal stress field; (3) grains are surrounded by deformable neighbors; (4) grain surfaces are modeled with a contact algorithm permitting grain-boundary cracking; (5) elastic properties and specific heat capacity vary with temperature [*Ackermann and Sorrell*, 1974; *Chon et al.*, 2003; *Connolly*, 2005; *Skinner*, 1966]; (6) the materials are compressible; and (7) a lithostatic confining pressure is applied to the sample boundaries (calculated as a linear function of depth with a constant crustal density of 2800 $kgm^{-3}$). Key differences between 2D calibration and 2D burial models are: in the burial models, (1) the rheology of the grains is augmented by viscous power-law flow (equation (14)); (2) in addition to thermal loading, the model surface experiences a lithostatic pressure load; (3) thermal-mechanical loading rate is determined by the sample's burial velocity, the employed geotherm, and the assumed crustal density; and (4) for simplicity, the model does not contain open grain-boundary cracks prior to burial. If not stated otherwise, we use the term 'stress' for von Mises' equivalent stress.

### 5.2. Results

[24] In the following, we restrict ourselves to simulations using a continental geotherm with a surface heat flow of 70 $mWm^{-2}$ and a burial velocity of 1 cm/a. The 1D and 2D results of the stress evolution are similar but there are interesting differences (Figures 9c and 9d). In the 2D case, we report mean deviatoric stresses for each mineral phase. In quartz, the magnitude of peak stress of the 2D solution is larger than in the 1D case. Geometric stress concentrations at highly arcuate grain boundaries and triple points increase mean deviatoric stress by a factor >2 (Figure 11). In contrast, peak stress in feldspars is lower in the 2D case. In the 1D model, the virtual partner mineral inducing thermal expansion mismatch is always quartz. In the 2D model, many feldspar grains abut other phases with lower thermal expansivities than quartz. As a result, local thermal mismatch and hence local internal stresses are smaller. Importantly, the partner minerals deform elastically and viscously. In particular, viscous relaxation of quartz at temperatures

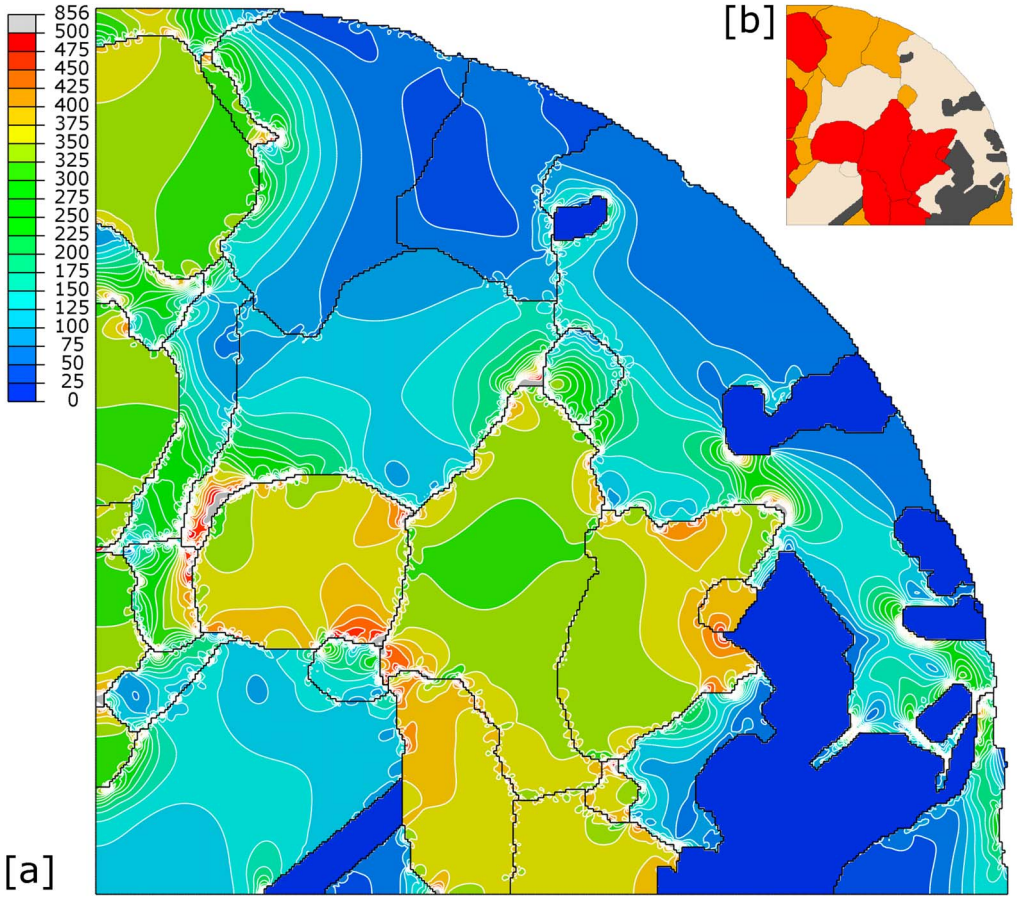


**Figure 11.** 2D numerical model of buried granite with a burial velocity of 0.01 m/a, and a geotherm according to a surface heat flow of 70 $mWm^{-2}$. Model is shown at peak stress in quartz, corresponding to a temperature of 360°C and depth of 17 km. (a) Contour plot of von Mises stress (color scale is in MPa). Note stress concentrations at arcuate grain boundaries and triple points. (b) Color-coded map showing the four mineral phases: quartz (dark red), plagioclase (light gray), microcline (orange), and mica (dark gray).

>360°C inhibits stress build-up in feldspars, as indicated by the change of slope of the stress curves (Figure 9d). Mica displays almost the same behavior in both models because of its pronounced weakness. The employed quasi-plastic flow law [*Kronenberg et al.*, 1990] suggests that it deforms inelastically at temperatures <100°C. In the 2D model, mica reaches a slightly higher peak stress at lower temperatures than in the 1D case. This is again due to the fact that, in the 1D case, all minerals were paired with quartz. At low temperatures, thermal expansion mismatch is higher for the pair feldspar-mica than for quartz-mica (Figure 4a). These results underline the notion that quartz controls thermally induced internal stresses in quartz- and feldspar-rich rocks [*Fredrich and Wong*, 1986; *Kranz*, 1983], not only due to its large expansivity but also due to its creep behavior. A plot of relaxation time over temperature (Figure 12a) calculated from the 2D burial model shows that internal stresses in quartz have relaxation times >1 ma at temperatures below 300°C. At 350°C, the relaxation time of quartz drops to below 100 ka. However, plagioclase displays relaxation times >1 ma up to temperatures of 450°C. This implies that buried granitic rocks may easily store deviatoric thermal-elastic stresses of order 100 MPa with relaxation times of order 1 ma at this temperature. The importance of thermal elasticity at temperatures >300°C is underlined by a comparison of dissipated and stored energy in our 2D burial model (Figure 12b). At temperatures >400°C, dissipated energy makes up <16% of the amount of stored energy. Note how steep increases in the proportion of dissipated energy coincide with the peak stress regimes of mica, quartz, and feldspar. It is also interesting to examine the history of grain boundary cracking in the 2D burial model. We find that grain-boundary cracking

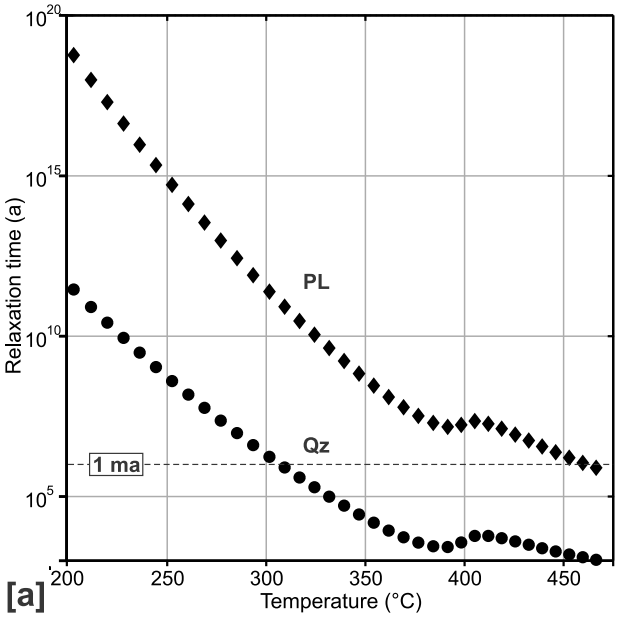


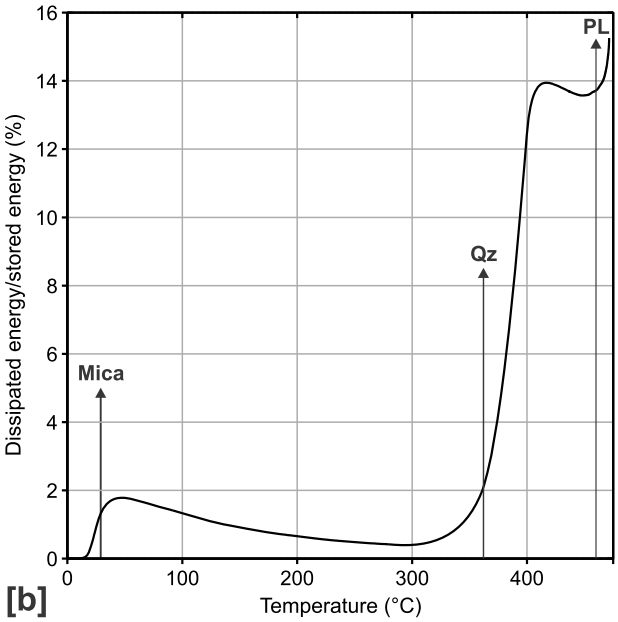


**Figure 12.** (a) Plot of relaxation time for quartz (circles) and plagioclase (diamonds) over temperature derived from the 2D burial model. Dashed horizontal line marks a relaxation time of 1 ma. (b) Plot of ratio of dissipated over stored energy in percent over temperature computed for the whole 2D burial model. Temperatures of peak stresses of mica, quartz, and plagioclase are marked with arrows.

is largely suppressed (Figure 13). Mean crack width is an order of magnitude smaller than in the experiment conducted under atmospheric pressure (compare Figure 8). Most notably, less than 1% of the available grain-boundary surface area cracks. This observation implies that grain-boundary cracking is a negligible dissipation mechanism under the conditions modeled here.

## 6. Discussion and Conclusions

[25] We now return to the hypothesis raised in the introduction. Based on extrapolations of the physical heating experiment through 1D semi-analytical and 2D burial simulations, we can give an affirmative answer: burial-induced deviatoric thermal-elastic stresses bring granitic continental crust close to failure at the grain scale. These internal stresses are expected to have important effects. First, they render buried rock in a highly pre-stressed state. Tectonic forces will thus lead to inelastic deformation, i.e., failure, of the material even at relatively low differential stresses. Moreover, grain-scale thermal-elastic

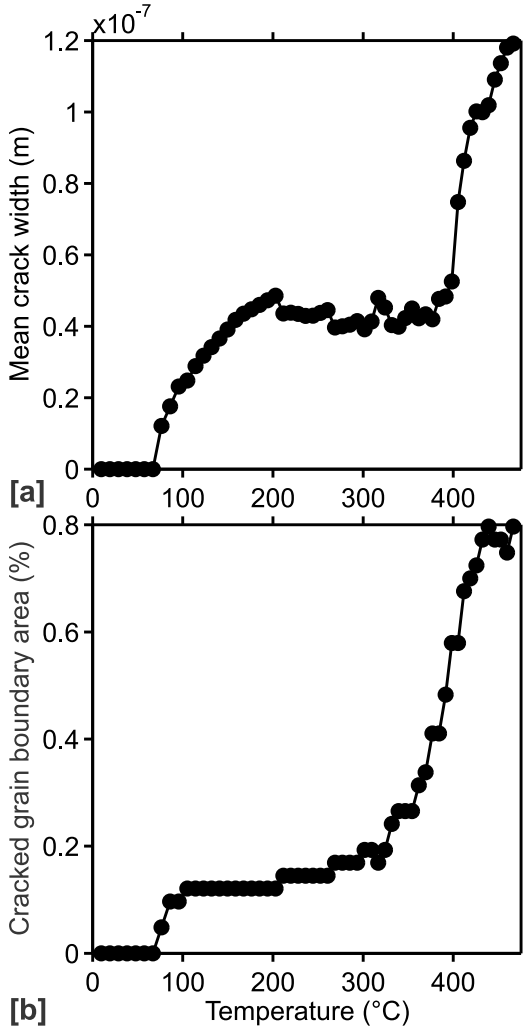


**Figure 13.** Plots of (a) mean grain-boundary crack width and (b) proportion of cracked grain boundaries over temperatures for 2D burial model.

stresses constitute large deviatoric stress perturbations, the length scale of which is related to the grain-size distribution of the rock. It is well known that local stress perturbations control fault nucleation and early fault linking [e.g., *Crider and Peacock*, 2004]. Therefore, it is expected that highly heterogeneous deviatoric internal stresses promote local grain-scale instabilities if buried rock is loaded tectonically, which in turn facilitates localized failure at larger scales under protracted far-field loading. *Regenauer-Lieb and Yuen* [2004] found that thermal elasticity promotes thermal-mechanical instabilities in lithospheric-scale numerical models of interacting ductile faults. The work at hand provides microphysical support for this hypothesis. Thermal-elastic stresses also matter at large scales, as shown, for example, for cooling plutons [*Bergbauer et al.*, 1998; *Savage*, 1978] and cooling oceanic plates [*Korenaga*, 2007a; *Parmentier and Haxby*, 1986; *Turcotte*, 1974]. Regardless of the length scale of a rock body, significant thermal-elastic stresses will always arise when sufficient temperature gradients (in time and/or space) occur because (1) rocks are generally spatially confined to some degree, meaning they cannot expand freely in all directions; and (2) rocks are heterogeneous materials exhibiting spatial variations in thermal-elastic material properties at all scales, from the grain scale, as shown here, to the lithospheric scale (e.g., a granitic intrusion in sedimentary host rocks). Our models imply that thermal-elastic stresses in buried quartzo-feldspathic rocks have relaxation times of order 1 ma up to a temperature of ∼450°C. However, the relaxation times and also the maximum magnitude of those stresses depend on model rheology. We employed a simple visco-elastic model. For viscous flow, power-law relations determined for steady-state flow were used. Yet it is possible that both quartz and feldspar may deform by high-stress transient creep mechanisms such as kinking and twinning in the low-temperature regime [*Carter and Kirby*, 1978; *Carter and Tsenn*, 1987]. Transient creep could therefore relax thermal-elastic stresses at temperatures below the power-law regime. For this type of rheology, a Burger's body could be used [e.g., *Chopra*, 1997]. However, we preferred the simpler Maxwell body for four reasons. First, it is very difficult to determine transient-creep rheologies for the minerals of interest experimentally over the pressure- and temperature range considered; hence, no reliable mechanical data are available. Second, the Maxwell rheology is employed routinely by geophysicists to describe the deformation of Earth materials [e.g., *Bailey*, 2006; *Kaus and Becker*, 2007; *Korenaga*, 2007b]. Third, it has been suggested that the critical stress, above which the breakdown of the power-law rheology occurs, is of order one hundredth of the shear modulus of the material in silicates [*Tsenn and Carter*, 1987]. For quartz, this critical stress is ∼400 MPa. Our results indicate that this high stress is achieved only locally once the sample reached its peak stress in quartz (Figure 11). The occurrence of this peak stress coincides with the onset of efficient power-law flow. Therefore, if *Tsenn and Carter*'s [1987] estimate of the critical stress for transient creep is correct, the latter does not matter in our study. Fourth, experiments on transient creep in dunite suggest that the ratio of the effective viscosities of transient over steady-state values lies between 0.17 and 0.67 and is relatively insensitive to temperature and stress [*Chopra*, 1997]. To our knowledge, this ratio is not constrained for quartz and feldspar. However, the variability of effective viscosities of quartz due to its sensitivity to water content is probably much greater than that possibly induced by transient creep. This can be seen in our 1D computations (Figure 9a), where we used two power-law relationships for quartz [*Hirth et al.*, 2001; *Rutter and Brodie*, 2004] that bracket the range of available flow laws. Hence, the uncertainty of the steady-state flow law for quartz is likely much larger than that induced by neglecting transient creep. In our 2D burial model, we applied the upper-bound dislocation creep law for wet quartz of *Rutter and Brodie* [2004]. Therefore, the relaxation times reported here should probably be regarded as upper-bound estimate.

[26] Another simplification of our rheological model is its neglect of intracrystalline and transcrystalline micro-cracking, i.e., plasticity of the grains themselves. Micro-cracking within and across grains might occur and contribute to stress relaxation in the brittle regime. However, we argue that this relaxation mechanism is likely of subordinate relevance in the case considered here. First, laboratory heating experiments at constant confining pressures show that above a confining pressure of ∼100 MPa, thermal-elastic micro-cracking is suppressed in granite [*Heard and Page*, 1982; *Wong and Brace*, 1979]. This pressure corresponds to a cut-off depth of ∼3–4 km for granitic crust and temperatures between ∼60 and 100°C. Therefore, micro-cracking should be negligible for most of the modeled pressure-temperature path. Moreover, our simulations permit intercrystalline plasticity through the use of contact mechanics: model grain boundaries can crack. We found that grain-boundary cracking is inhibited

when both temperature and confining pressure increase gradually (Figure 13). In addition, Figure 9 shows that, even if we assumed unrealistically that thermal-elastic stresses accumulated between the surface and the cut-off depth for micro-cracking were fully relaxed by micro-cracking, the peak stress would decrease by ~10% at the most. We therefore infer that micro-cracking is negligible as efficient stress relaxation mechanism in buried granitic rock, at least in the absence of pore fluid and external tectonic loading.

[27] However, in nature, additional stress relaxation processes occur. As implied in the preceding paragraph, brittle damage and thus stress relaxation may occur even under high confining pressures if tectonic stresses are applied, promoted by the presence of water [*Hall and Bodnar*, 1989; *Kranz*, 1983; *Meredith and Atkinson*, 1985]. Moreover, superposing far-field stresses (e.g., due to tectonics or topography) would decrease effective viscosity in power-law materials and reduce relaxation times [e.g., *Buergmann and Dresen*, 2008]. Metamorphic reactions may relax thermal-elastic stresses. Thermal-elastic stresses might even promote chemical reactions and diffusive mass transfer on the grain scale due to high grain-boundary contact stresses [*Gray and Durney*, 1979; *Wheeler*, 1987]. In summary, the magnitude and longevity of thermal-elastic stresses in actively deforming systems depend on many additional factors such as far-field stresses, water content, deformation mechanisms, chemical reactions etc. However, we neglected these factors deliberately to estimate the contribution of thermal elasticity to burial-induced grain-scale stresses alone.

[28] In conclusion, we simulated the grain-scale stress field that is induced in granitic rock by slow burial with a workflow combining physical heating experiments with 1D and 2D numerical models. Our 2D burial models account for the effects of microstructure, dissipative grain boundaries, contact stresses, thermal-expansion as well as elastic mismatch, temperature-dependent thermal-elastic material properties, and viscous relaxation. The results imply that thermal-elastic stresses affect the continental crust on geological time scales, from hundreds of thousands to millions of years. Thermal elasticity may bring the continental crust close to failure at the grain scale, especially near the brittle-ductile transition. Large grain-scale perturbations of deviatoric stress may provide the potential trigger for an upward cascade of instabilities under an applied large-scale load. We thus have identified an important intrinsic mechanism for the nucleation of crustal-scale instabilities. Thermal elasticity acts as a fundamental booster for brittle-ductile failure.

## Acknowledgments

[29] C. Schrank is thankful for funding by the German Research Foundation (DFG) under grant SCHR 1262/1–1. This work was supported by the Western Australian State Government through the Premier's Fellowship and the Western Australian Geothermal Centre of Excellence Program. The Commonwealth of Australia supported this work under the Major National Research Facilities Program and the Australian Synchrotron Research Program. Use of the Advanced Photon Source at Argonne National Laboratory was supported by the U. S. Department of Energy, Office of Science, Office of Basic Energy Sciences, under contract DE-AC02-06CH11357. We are grateful to F. De Carlo and X. Xiao from sector 2-BM at APS for supplying the heating equipment used in this experiment, and acknowledge iVEC in Perth for help with visualization. S. Revets is thanked for Perplex calculations and J. Mecklenburgh for comments on a previous version of the paper. We thank the editor Joel Baker and two anonymous referees for their constructive comments.

## References

Ackermann, R. J., and C. A. Sorrell (1974), Thermal expansion and the high-low transformation in quartz. I. High-temperature X-ray studies, *J. Appl. Crystallogr.*, *7*(5), 461–467, doi:10.1107/S0021889874010211.

Bailey, R. C. (2006), Large time step numerical modelling of the flow of Maxwell materials, *Geophys. J. Int.*, *164*(2), 460–466, doi:10.1111/j.1365-246X.2005.02788.x.

Bass, J. D. (1995), Elasticity of minerals, glasses, and melts, in *Mineral Physics & Crystallography: A Handbook of Physical Constants*, *AGU Ref. Shelf*, vol. 2, edited by T. J. Ahrens, pp. 45–63, AGU, Washington, D. C., doi:10.1029/RF002p0045.

Ben-Zion, Y., and P. Leary (1986), Thermoelastic strain in a half-space covered by unconsolidated material, *Bull. Seismol. Soc. Am.*, *76*(5), 1447–1460.

Bergbauer, S., S. J. Martel, and C. F. Hieronymus (1998), Thermal stress evolution in cooling pluton environments of different geometries, *Geophys. Res. Lett.*, *25*(5), 707–710, doi:10.1029/98GL00047.

Berman, R. G. (1988), Internally consistent thermodynamic data for minerals in the system Na2O–K2O-CaO-MgO-FeO-Fe2O3-Al2O3-SiO2-TiO2–H2O-CO2, *J. Petrol.*, *29*(2), 445–522.

Blacic, J. D. (1981), Water diffusion in quartz at high pressure: Tectonic implications, *Geophys. Res. Lett.*, *8*(7), 721–724, doi:10.1029/GL008i007p00721.

Blendell, J. E., and R. L. Coble (1982), Measurement of stress due to thermal expansion anisotropy in Al2O3, *J. Am. Ceram. Soc.*, *65*(3), 174–178, doi:10.1111/j.1151-2916.1982.tb10390.x.

Brace, W. F., and D. L. Kohlstedt (1980), Limits on lithospheric stress imposed by laboratory experiments, *J. Geophys. Res.*, *85*(B11), 6248–6252, doi:10.1029/JB085iB11p06248.

Bratt, S. R., E. A. Bergman, and S. C. Solomon (1985), Thermoelastic stress: How important as a cause of earthquakes in

young oceanic lithosphere?, *J. Geophys. Res.*, *90*(B12), 10,249–10,260, doi:10.1029/JB090iB12p10249.

Bruner, W. M. (1979), Crack growth and the thermoelastic behavior of rocks, *J. Geophys. Res.*, *84*(B10), 5578–5590, doi:10.1029/JB084iB10p05578.

Bruner, W. M. (1984), Crack growth during unroofing of crustal rocks: Effects on thermoelastic behavior and near-surface stresses, *J. Geophys. Res.*, *89*(B6), 4167–4184, doi:10.1029/JB089iB06p04167.

Buergmann, R., and G. Dresen (2008), Rheology of the lower crust and upper mantle: Evidence from rock mechanics, geodesy, and field observations, *Ann. Rev. Earth Planet. Sci.*, *36*, 531–567.

Carter, N. L., and S. H. Kirby (1978), Transient creep and semibrittle behavior of crystalline rocks, *Pure Appl. Geophys.*, *116*(4–5), 807–839, doi:10.1007/BF00876540.

Carter, N. L., and M. C. Tsenn (1987), Flow properties of continental lithosphere, *Tectonophysics*, *136*(1–2), 27–63, doi:10.1016/0040-1951(87)90333-7.

Chon, C.-M., S. A. Kim, and H.-S. Moon (2003), Crystal structures of biotite at high temperatures and of heat-treated biotite using neutron powder diffraction, *Clays Clay Miner.*, *51*(5), 519–528, doi:10.1346/CCMN.2003.0510506.

Chopra, P. N. (1997), High-temperature transient creep in olivine rocks, *Tectonophysics*, *279*(1–4), 93–111, doi:10.1016/S0040-1951(97)00134-0.

Clauser, C., and E. Huenges (1995), Thermal conductivity of rocks and minerals, in *Rock Physics & Phase Relations: A Handbook of Physical Constants*, *AGU Ref. Shelf*, vol. 3, edited by T. J. Ahrens, pp. 105–126, AGU, Washington, D. C., doi:10.1029/RF003p0105.

Connolly, J. A. D. (2005), Computation of phase equilibria by linear programming: A tool for geodynamic modeling and its application to subduction zone decarbonation, *Earth Planet. Sci. Lett.*, *236*(1–2), 524–541, doi:10.1016/j.epsl.2005.04.033.

Cooper, H. W., and G. Simmons (1977), The effect of cracks on the thermal expansion of rocks, *Earth Planet. Sci. Lett.*, *36*(3), 404–412, doi:10.1016/0012-821X(77)90065-6.

Crider, J. G., and D. C. P. Peacock (2004), Initiation of brittle faults in the upper crust: A review of field observations, *J. Struct. Geol.*, *26*(4), 691–707, doi:10.1016/j.jsg.2003.07.007.

Darot, M., Y. Gueguen, and M.-L. Baratin (1992), Permeability of thermally cracked granite, *Geophys. Res. Lett.*, *19*(9), 869–872, doi:10.1029/92GL00579.

Denlinger, R. P., and W. Z. Savage (1989), Thermal stresses due to cooling of a viscoelastic oceanic lithosphere, *J. Geophys. Res.*, *94*(B1), 744–752, doi:10.1029/JB094iB01p00744.

Eberhardt, E., B. Stimpson, and D. Stead (1999), Effects of grain size on the initiation and propagation thresholds of stress-induced brittle fractures, *Rock Mech. Rock Eng.*, *32*(2), 81–99, doi:10.1007/s006030050026.

Escher, A., and C. Beaumont (1997), Formation, burial and exhumation of basement nappes at crustal scale: A geometric model based on the Western Swiss-Italian Alps, *J. Struct. Geol.*, *19*(7), 955–974, doi:10.1016/S0191-8141(97)00022-9.

Evans, A. G. (1978), Microfracture from thermal expansion anisotropy–I. Single phase systems, *Acta Metall.*, *26*(12), 1845–1853, doi:10.1016/0001-6160(78)90097-4.

Fowler, C. M. R. (1990), *The Solid Earth: An Introduction to Global Geophysics*, 1st ed., 472 pp., Cambridge Univ. Press, Cambridge, U. K.

Fredrich, J. T., and T.-F. Wong (1986), Micromechanics of thermally induced cracking in three crustal rocks, *J. Geophys. Res.*, *91*(B12), 12,743–12,764, doi:10.1029/JB091iB12p12743.

Goetze, C., and B. Evans (1979), Stress and temperature in the bending lithosphere as constrained by experimental rock mechanics, *Geophys. J. R. Astron. Soc.*, *59*(3), 463–478, doi:10.1111/j.1365-246X.1979.tb02567.x.

Gray, D. R., and D. W. Durney (1979), Crenulation cleavage differentiation: Implications of solution-deposition processes, *J. Struct. Geol.*, *1*(1), 73–80, doi:10.1016/0191-8141(79)90023-3.

Hadley, K. (1976), Comparison of calculated and observed crack densities and seismic velocities in Westerly granite, *J. Geophys. Res.*, *81*(20), 3484–3494, doi:10.1029/JB081i020p03484.

Hall, D. L., and R. J. Bodnar (1989), Comparison of fluid inclusion decrepitation and acoustic emission profiles of Westerly granite and Sioux quartzite, *Tectonophysics*, *168*(4), 283–296, doi:10.1016/0040-1951(89)90223-0.

Hashin, Z., and S. Shtrikman (1963), A variational approach to the theory of the elastic behaviour of multiphase materials, *J. Mech. Phys. Solids*, *11*(2), 127–140, doi:10.1016/0022-5096(63)90060-7.

Heard, H. C., and L. Page (1982), Elastic moduli, thermal expansion, and inferred permeability of two granites to 350°C and 55 megapascals, *J. Geophys. Res.*, *87*(B11), 9340–9348, doi:10.1029/JB087iB11p09340.

Hibbit, Karlsson and Sorenson (2009), *ABAQUS/Standard User's Manual, Version 6.9*, Pawtucket, R. I.

Hirth, G., C. Teyssier, and J. Dunlap (2001), An evaluation of quartzite flow laws based on comparisons between experimentally and naturally deformed rocks, *Int. J. Earth Sci.*, *90*(1), 77–87, doi:10.1007/s005310000152.

Jaumann, G. (1911), Geschlossenes System physikalischer und chemischer Differential-Gesetze, *Sitzber. Akad. Wiss. Wien, Abt. IIa*, *120*, 385–530.

Karrech, A., D. Duhamel, G. Bonnet, F. Chevoir, J. N. Roux, J. Canou, and J. C. Dupla (2008), A discrete element study of settlement in vibrated granular layers: Role of contact loss and acceleration, *Granul. Matter*, *10*(5), 369–375, doi:10.1007/s10035-008-0101-7.

Kaus, B. J. P., and T. W. Becker (2007), Effects of elasticity on the Rayleigh–Taylor instability: Implications for large-scale geodynamics, *Geophys. J. Int.*, *168*(2), 843–862, doi:10.1111/j.1365-246X.2006.03201.x.

Knackstedt, M. A., C. H. Arns, M. Saadatfar, T. J. Senden, A. Limaye, A. Sakellariou, A. P. Sheppard, R. M. Sok, W. Schrof, and H. Steininger (2006), Elastic and transport properties of cellular solids derived from three-dimensional tomographic images, *Proc. R. Soc. A*, *462*(2073), 2833–2862.

Korenaga, J. (2007a), Thermal cracking and the deep hydration of oceanic lithosphere: A key to the generation of plate tectonics?, *J. Geophys. Res.*, *112*(B5), B05408, doi:10.1029/2006JB004502.

Korenaga, J. (2007b), Effective thermal expansivity of Maxwellian oceanic lithosphere, *Earth Planet. Sci. Lett.*, *257*(1–2), 343–349, doi:10.1016/j.epsl.2007.03.010.

Kranz, R. L. (1983), Microcracks in rocks: A review, *Tectonophysics*, *100*(1–3), 449–480, doi:10.1016/0040-1951(83)90198-1.

Kronenberg, A. K., S. H. Kirby, and J. Pinkston (1990), Basal slip and mechanical anisotropy of biotite, *J. Geophys. Res.*, *95*(B12), 19,257–19,278, doi:10.1029/JB095iB12p19257.

Lapen, T. J., C. M. Johnson, L. P. Baumgartner, N. J. Mahlen, B. L. Beard, and J. M. Amato (2003), Burial rates during prograde metamorphism of an ultra-high-pressure terrane: An example from Lago di Cignana, western Alps, Italy, *Earth*

*Planet. Sci. Lett.*, *215*(1–2), 57–72, doi:10.1016/S0012-821X(03)00455-2.

Meredith, P. G., and B. K. Atkinson (1985), Fracture toughness and subcritical crack growth during high-temperature tensile deformation of Westerly granite and Black gabbro, *Phys. Earth Planet. Inter.*, *39*(1), 33–51, doi:10.1016/0031-9201(85)90113-X.

Moore, D. E., and D. A. Lockner (1995), The role of microcracking in shear-fracture propagation in granite, *J. Struct. Geol.*, *17*(1), 95–114, doi:10.1016/0191-8141(94)E0018-T.

Nadan, B. J., and T. Engelder (2009), Microcracks in New England granitoids: A record of thermoelastic relaxation during exhumation of intracontinental crust, *Geol. Soc. Am. Bull.*, *121*(1–2), 80–99.

Nasseri, M. H. B., A. Schubnel, and R. P. Young (2007), Coupled evolutions of fracture toughness and elastic wave velocities at high crack density in thermally treated Westerly granite, *Int. J. Rock Mech. Min. Sci.*, *44*(4), 601–616, doi:10.1016/j.ijrmms.2006.09.008.

Nasseri, M. H. B., A. Schubnel, P. M. Benson, and R. P. Young (2009), Common evolution of mechanical and transport properties in thermally cracked westerly granite at elevated hydrostatic pressure, *Pure Appl. Geophys.*, *166*(5–7), 927–948, doi:10.1007/s00024-009-0485-2.

Parmentier, E. M., and W. F. Haxby (1986), Thermal stresses in the oceanic lithosphere: Evidence from geoid anomalies at fracture zones, *J. Geophys. Res.*, *91*(B7), 7193–7204, doi:10.1029/JB091iB07p07193.

Regenauer-Lieb, K. (2006), Water and geodynamics, *Rev. Mineral. Geochem.*, *62*, 451–473, doi:10.2138/rmg.2006.62.19.

Regenauer-Lieb, K., and D. A. Yuen (2003), Modeling shear zones in geological and planetary sciences: Solid- and fluid-thermal-mechanical approaches, *Earth Sci. Rev.*, *63*(3–4), 295–349, doi:10.1016/S0012-8252(03)00038-2.

Regenauer-Lieb, K., and D. Yuen (2004), Positive feedback of interacting ductile faults from coupling of equation of state, rheology and thermal-mechanics, *Phys. Earth Planet. Inter.*, *142*(1–2), 113–135, doi:10.1016/j.pepi.2004.01.003.

Richter, D., and G. Simmons (1974), Thermal expansion behavior of igneous rocks, *Int. J. Mech. Min. Sci. Geomech. Abstr.*, *11*(10), 403–411, doi:10.1016/0148-9062(74)91111-5.

Rosen, B. W., and Z. Hashin (1970), Effective thermal expansion coefficients and specific heats of composite materials, *Int. J. Eng. Sci.*, *8*(2), 157–173, doi:10.1016/0020-7225(70)90066-2.

Rutter, E. H., and K. H. Brodie (2004), Experimental intracrystalline plastic flow in hot-pressed synthetic quartzite prepared from Brazilian quartz crystals, *J. Struct. Geol.*, *26*(2), 259–270, doi:10.1016/S0191-8141(03)00096-8.

Rybacki, E., and G. Dresen (2000), Dislocation and diffusion creep of synthetic anorthite aggregates, *J. Geophys. Res.*, *105*(B11), 26,017–26,036, doi:10.1029/2000JB900223.

Savage, W. Z. (1978), The development of residual stress in cooling rock bodies, *Geophys. Res. Lett.*, *5*(8), 633–636, doi:10.1029/GL005i008p00633.

Skinner, B. J. (1966), Thermal expansion, in *Handbook of Physical Constants*, edited by S. P. J. Clark, pp. 75–96, Geol. Soc. of Am., Boulder, Colo.

Tromans, D., and J. A. Meech (2004), Fracture toughness and surface energies of covalent minerals: Theoretical estimates, *Miner. Eng.*, *17*(1), 1–15, doi:10.1016/j.mineng.2003.09.006.

Tsenn, M. C., and N. L. Carter (1987), Upper limits of power law creep of rocks, *Tectonophysics*, *136*(1–2), 1–26, doi:10.1016/0040-1951(87)90332-5.

Turcotte, D. L. (1974), Are transform faults thermal contraction cracks?, *J. Geophys. Res.*, *79*(17), 2573–2577, doi:10.1029/JB079i017p02573.

Turcotte, D. L., and E. R. Oxburgh (1976), Stress accumulation in the lithosphere, *Tectonophysics*, *35*(1–3), 183–199, doi:10.1016/0040-1951(76)90037-8.

Walsh, J. B. (1973), Theoretical bounds for thermal expansion, specific heat, and strain energy due to internal stress, *J. Geophys. Res.*, *78*(32), 7637–7646, doi:10.1029/JB078i032p07637.

Wheeler, J. (1987), The significance of grain-scale stresses in the kinetics of metamorphism, *Contrib. Mineral. Petrol.*, *97*(3), 397–404, doi:10.1007/BF00372002.

Wong, T.-F., and W. F. Brace (1979), Thermal expansion of rocks: Some measurements at high pressure, *Tectonophysics*, *57*(2–4), 95–117, doi:10.1016/0040-1951(79)90143-4.

Zang, A. (1993), Finite element study on the closure of thermal microcracks in feldspar/quartz-rocks—I. Grain-boundary cracks, *Geophys. J. Int.*, *113*(1), 17–31, doi:10.1111/j.1365-246X.1993.tb02525.x.

Zoback, M. D., et al. (1993), Upper-crustal strength inferred from stress measurements to 6 km depth in the KTB borehole, *Nature*, *365*(6447), 633–635, doi:10.1038/365633a0.